EVALUATING THE EFFECTS OF SPATIAL RESOLUTION ON HYPERSPECTRAL FIRE DETECTION AND TEMPERATURE RETRIEVAL

by

Daniel Scott Matheson

A thesis submitted to the faculty of
The University of Utah
in partial fulfillment of the requirements for the degree of

Master of Science

Department of Geography

University of Utah

August 2011

The University of Utah Graduate School

STATEMENT OF THESIS APPROVAL

The thesis of **Daniel Scott Matheson**

has been approved by the following supervisory committee members:

Philip E. Dennison	, Chair	**05/12/2011** Date Approved
Richard R. Forster	, Member	**05/12/2011** Date Approved
Thomas J. Cova	, Member	**05/12/2011** Date Approved

and by **George F. Hepner** , Chair of the Department of **Geography**

and by Charles A. Wight, Dean of The Graduate School.

ABSTRACT

Hyperspectral remote sensing of wildfires combines principles of emitted radiation with advanced spectrometry to model wildfire area and temperature, as well as background land cover classification, at the subpixel level. Yet airborne hyperspectral sensors face problems of inconsistent spatial resolutions and have limited spatial and temporal coverage. A proposed hyperspectral/thermal infrared satellite, the Hyperspectral InfraRed Imager (HyspIRI), will provide hyperspectral data over a spectral range of 350-2500 nm at a spatial resolution of 60.0 m. Hyperspectral radiance data have previously been shown to allow fire detection and retrieval of fire temperature, although these abilities have not been demonstrated at spatial resolutions coarser than 16.1 m. For this study, four hyperspectral images containing active fires were acquired by the Airborne Visible-Infrared Imaging Spectrometer (AVIRIS), with spatial resolutions ranging from 3.8 to 16.1 m. By resampling these AVIRIS images to coarser spatial resolutions and by modeling fire area, fire temperatures and background land cover, the impacts of spatial resolution on fire detection and temperature retrieval were simulated. Multiple endmember spectral mixture analysis (MESMA) methods were used to model fire temperature and background land cover types. Modeling at coarser spatial resolutions produced larger areas of low fire temperatures with lower modeling error than modeling at finer spatial resolutions. Modeling results comparing 60.0 m data with and without a Gaussian point spread function validated pixel aggregation resampling as a suitable approximation of coarser spatial resolution imagery. Coarser spatial resolution

hyperspectral data, such as that collected by the future HyspIRI sensor, are likely to model more fire area and lower temperatures when compared against simultaneously acquired higher spatial resolution data. Increasing the saturation thresholds of SWIR channels could greatly improve the fire detection and temperature modeling capabilities of a HyspIRI-like sensor.

TABLE OF CONTENTS

LIST OF TABLES

LIST OF FIGURES

ACKNOWLEDGEMENTS

I would like to thank my adviser, Dr. Philip Dennison, for his tireless efforts on my behalf. He was incredibly patient with me during each step of this process, selflessly offered his time to help me make progress, and served as a constant inspiration for excellence. He provided the funding, the raw data, and generated almost all of the code for this research. I couldn't have asked for a better adviser.

I would like to thank my committee, Dr. Thomas Cova and Dr. Richard Forster, for their friendship and encouragement along the way. I also want to thank them for their expertise in the areas of wildfires and remote sensing, respectively, and for their helpful suggestions that made this research more scientifically thorough. I would also like to thank the National Geospatial Intelligence Agency for funding this academic research, and for offering me a job!

My gratitude also extends to the faculty and staff in the Department of Geography for their service, their examples, and their words of encouragement. I am also grateful for my fellow students, many of whom will remain my close friends for years to come. I can't thank them enough for their friendship, their indomitable spirits in the face of insurmountable softball odds, their laughter, and their constant support.

Finally, I would like to thank my family. To Mom and Dad: Thanks for your inspiring encouragement and unconditional love. To my siblings, especially my brother Ross, who has always been an inspiration to me, but even more so after he has battled severe health problems over the last two years. To my grandparents, two of whom I lost

during the course of this research: Thank you for giving me a lifelong perspective on the value of hard work and service. And of course to my loving wife Cathryn, to whom I owe my sincerest thanks and deepest admiration: Thank you for your daily sustaining support, your mad editing skills, for keeping the gravy train rolling even while pregnant with our son, and for your genuine interest and constant motivation. There isn't a luckier guy in the world.

1 INTRODUCTION

Wildfires are a growing problem in the United States, especially as the wildland-urban interface continues to expand. The average annual area burned over the last nine years was a considerable 28,504 km^2, compared to an annual area of 16,858 km^2 over the last 50 years (National Interagency Fire Center, 2010). In addition to endangering human life and disturbing ecosystems, wildfires emit large amounts of pollutants, including CO_2, into the atmosphere. The negative impacts of wildfires add to already growing concerns regarding the carbon cycle and global climate change.

Remote sensing has appropriately become a tool of choice for examining and evaluating the effects of wildfires on the environment. This is due to its ability to easily map fires and fire impacts over large areas. Its ability to measure reflected and emitted electromagnetic radiation at high spectral resolutions provides valuable information on the impacts of fire on vegetation (e.g., Drewa et al., 2002), soils (e.g., Kokaly et al., 2007), and potentially even behavior of active fires (e.g., Riaño et al., 2003). Although remotely sensed information represents a snapshot in time, repeat acquisitions allow researchers to detect change and discern patterns over time, such as the regeneration of vegetation in a burned area.

One specific type of remote sensing, hyperspectral imaging, is a growing research area which can provide much needed information for studying wildfires and their behavior. Hyperspectral sensors are imaging spectrometers which measure the distinct spectral responses of various phenomena of interest based on their physical or chemical

properties (Jensen, 2007). Hyperspectral sensors have many contiguous spectral bands—hundreds, compared to the dozen or fewer typical on most sensors—that can measure large portions of the electromagnetic spectrum. This information allows researchers to discriminate between different objects or land cover types in an image. Applications of hyperspectral remote sensing include image classification and vegetation mapping (e.g., Hoefen et al., 2010), change detection (e.g., Canty, 2009), and more recently fire detection and temperature mapping (Dennison & Roberts, 2009; Dennison et al., 2006).

Hyperspectral data improve upon another major application of remote sensing—modeling of mixtures of multiple radiance signals comprising a single pixel (e.g., Adams et al., 1993). The large number of bands allows percentages of land cover types to be calculated within each pixel, which can then be used to calculate the total fractional area of each land cover type. The Advanced Visible Infrared Imaging Spectrometer (AVIRIS) is a widely used airborne hyperspectral sensor, with 224 contiguous spectral bands recording electromagnetic data at 10 nm increments between approximately 400 and 2500 nm (Vane et al., 1984). AVIRIS has a spatial resolution ranging from 4.0 m to 20.0 m, depending on the altitude of the sensor.

Hyperspectral remote sensing of wildfires combines principles of emitted radiation with advanced spectrometry to model wildfire size and temperature, as well as background land cover classification, at the subpixel level. Yet AVIRIS, like all airborne sensors, faces problems of varying spatial resolutions, and has limited spatial and temporal coverage. The National Research Council Decadal Survey on NASA Earth science applications recommended the development of a hyperspectral/thermal infrared Tier 2 satellite mission (National Research Council, 2007). The proposed Hyperspectral

InfraRed Imager (HyspIRI) is currently in design stage at NASA. The VSWIR hyperspectral sensor proposed for HyspIRI is being designed to measure data contiguously across the range of 380 – 2500 nm at 10 nm increments, with a proposed spatial resolution of 60.0 m. With spectral capabilities similar to AVIRIS, HyspIRI will have the potential to detect fires and to retrieve fire temperature, although these abilities have not been demonstrated at the relatively coarse spatial resolution of 60.0 m. By resampling AVIRIS images to coarser spatial resolutions and modeling fire area, fire temperatures and background land cover, the impacts of spatial resolution on fire detection and temperature modeling can be simulated.

This study had four principle objectives: (1) To resample four AVIRIS images with active wildfires to spatial resolutions ranging from their initial resolution to approximately 60.0 m; (2) to observe and assess the performance of fire detection and temperature modeling on images resampled to coarser spatial resolutions; (3) to apply a Gaussian point spread function to one fire image to better simulate actual imagery from the planned HyspIRI VSWIR sensor, and assess the performance of the fire detection and background modeling at 60.0 m; and (4) to determine whether there is a threshold within the range (4.0–60.0 m) beyond which fire detection and temperature modeling are too inconsistent or are no longer useful. By addressing each of these objectives, it was hoped that significant trends could be noted and information presented to NASA scientists and collaborative researchers which are relevant to HyspIRI development, while the sensor is still in its design stage.

2 BACKGROUND

Remote sensing instruments measure electromagnetic energy reflected from or emitted by an object. For emitted radiation, colder temperature objects (i.e., background temperatures ranging from 300–500 K) emit most of their radiance in the thermal infrared (8–12 μm) and middle infrared (3–5 μm) regions of the electromagnetic spectrum. Hotter temperature objects (i.e., smoldering and flaming combustion above temperatures of 500 K) emit more of their radiance in the shortwave infrared (SWIR) portion of the spectrum (1.4–2.5 μm). Planck's Law calculates emitted blackbody radiance at a specific wavelength for a surface at a certain temperature. If radiance is known and a blackbody is assumed, the radiative temperature of the object can be estimated using Planck's Law.

Temperature modeling for wildfires is complicated, however, by the fact that most fire pixels are mixed, containing an averaged spectral radiance value for fire and nonfire areas. Additionally, there may be multiple flames present within a single pixel which emit at different temperatures. Subpixel area of fire and background land cover can be modeled using spectral mixing models, which estimate the fractions and spectral radiances of endmembers. Endmembers are spectrally pure signatures of a given land cover type (or specific fire temperature, in the case of wildfires), gathered from either field-measured spectra, relatively pure pixels in the image, or modeled radiance that accounts for atmospheric effects through radiative transfer modeling (Eckmann et al., 2008). The general equation for spectral mixing is:

$$L_{mix} = \sum_{i=0}^{n} f_i L_i \quad (1)$$

where L_i is the spectral radiance of each endmember, f_i is the fractional area of each endmember in the pixel, and L_{mix} is the total mixed spectral radiance for the pixel. In the case of modeling fire in SWIR wavelengths, the fraction and radiance terms can represent reflected solar radiance or emitted radiance from a fire. The first spectral mixing model applied to temperature retrieval of wildfires was developed by Dozier (1981) for the Advanced Very High Resolution Radiometer (AVHRR), which has a 1.1 km spatial resolution. This method uses a two endmember case which employs two broadband AVHRR channels at 4 µm and 11 µm to spectrally discriminate between fire and nonfire (cool background) endmembers. The method uses the following equation:

$$L_\lambda = f_{fire}\beta(\lambda, T_{fire}) + f_{background}\beta(\lambda, T_{background}) \quad (2)$$

where L_λ is the spectral radiance at a wavelength λ, f_{fire} and $f_{background}$ are the respective fractional areas of fire and background, $\beta(\lambda, T)$ is a Planck function, and T_{fire} and $T_{background}$ are the temperatures of the fire and the background, respectively. Eckmann et al. (2008) note that the method is based on the following assumptions: all objects and background emit as blackbodies, a hot object has a single, uniform temperature, and that atmospheric effects are minimal.

In light of these limitations, the Dozier (1981) method has been altered for various applications. Giglio et al. (2003) provided an alternative method using fire radiative power (FRP) for the Moderate-Resolution Imaging Spectroradiometer (MODIS) satellite,

similarly using the ratio of increased radiance between 4 μm and 11 μm wavelengths to detect fire pixels. Improvements were made upon the method by using a combination of shortwave bands (e.g., Green, 1996; Giglio et al., 2003; Dennison et al., 2006). Giglio and Kendall (2001) improved the method by generating a three endmember linear mixing model, which includes a reflected solar radiance fraction and a shade radiance, which contains scattered radiance from the atmosphere. The fraction and the shade radiance allow the fractional areas to fluctuate separately, thereby enhancing the model.

2.1 Fire Detection in Hyperspectral Data

With a closer look at hyperspectral fire modeling, there have been several previous applications of fire detection and both temperature and land cover modeling. Concerning fire detection, three indices using AVIRIS spectral bands have been proposed. Vodacek et al. (2002) proposed a potassium emission index based on a near infrared band combination (of 770 and 780 nm), which highlights a potassium emission feature that implies burning vegetation. Dennison (2006) introduced a carbon dioxide absorption index using a combination of three bands to indicate reduced CO_2 absorption caused by the limited path length of emitted radiance. Both indices are based on fine spectral features and prone to background noise (Dennison & Roberts, 2009).

Dennison and Roberts (2009) used kappa matrices to compare all potential combinations of AVIRIS bands, and termed the most accurate combination (two bands centered at 2061 and 2429 nm) the Hyperspectral Fire Detection Index (HFDI). They then evaluated the performance of HFDI against the potassium emission index (Vodacek et al., 2002) and the carbon dioxide emission index (Dennison, 2006) on AVIRIS scenes of the 2007 Zaca Fire and the 2008 Indians Fire in California (Fig. 1). They found that

HFDI outperformed the other indices, producing less background noise. Yet despite this success, the authors did find that the new index showed significantly lower accuracy when modeling temperatures below normal flaming combustion temperatures (below 750 K) and for the very hottest fire temperatures (above 1400 K). Dennison and Roberts (2009) recommend that HFDI be used in conjunction with additional temperature modeling methods, and that further investigation be conducted to assess the performance of HFDI at coarser spatial resolutions for future satellite hyperspectral sensors (e.g., HyspIRI).

2.2 Hyperspectral Temperature Modeling

There have also been previous temperature modeling applications using SWIR hyperspectral data. Green (1996) used observable spectral differences between emitted radiance and reflected solar radiance to model temperature. Dennison et al. (2006) improved upon the Green (1996) methods by applying multiple endmember spectral mixture analysis (MESMA; Roberts et al., 1998) to modeling fire temperatures. This method involves a spectral library of endmembers, and establishes the best fit combination of endmembers for each image spectrum. Dennison et al. (2006) used MESMA to compare and select the best fit combination of a reflected solar radiance endmember (from a spectral library of selected image endmembers), an emitted radiance endmember (from a spectral library of modeled emitted radiance endmembers for temperatures ranging from 500–1500 K), and a shade (no measured radiance) endmember. While the method was computationally intensive and produced some errors due to smoke and sensor saturation in the SWIR, it effectively combined temperature modeling and fire fractional area with background land cover classification. Dennison

and Matheson (2011) improved upon the Dennison et al. (2006) fire temperature modeling by using HFDI for fire detection, as well as separate spectral libraries of background endmembers for smoke, nonsmoke, and fire pixels. They compared similar modeling methods using imagery from both AVIRIS and the MODIS/ASTER Airborne Simulator (MASTER), acquired simultaneously onboard a NASA ER-2 platform flying over the 2008 Indians Fire in central coastal California, USA. This study assessed differences in fire detection and temperature retrieval when applied to hyperspectral and multispectral data, but did not examine the potential effects the two sensors' different spatial scales had on the modeling.

2.3 Spatial Rescaling

A primary limitation on the ability to characterize land cover or model temperatures in remotely sensed imagery is the spatial resolution of the imagery itself. Coarser spatial resolutions can result in a loss of spatial and spectral information, and spatial resolution effects are a frequent research question in the field of remote sensing. Ling (1997) found that variability among the values of a Landsat TM reflectance/ absorptance biomass index decreased with coarsening spatial resolution. Walsh et al. (1997) also demonstrated that biomass variation was scale dependent, noting a smoothing of NDVI values at coarser resolutions.

There have been many studies that have used multiscale approaches to examine vegetation and temperature retrieval, respectively. Anderson et al. (2007) used data with differing spatial scales acquired from airborne and spaceborne sensors to produce a land-atmosphere transfer scheme to compare changes in land temperatures at high temporal and spatial resolutions. Three-endmember modeling methods similar to those used by

Dennison et al. (2006) were used to assess subpixel fire properties in MODIS data (Eckmann et al., 2008; Eckmann et al., 2009; Eckmann et al., 2010). In these studies, fire area modeled from the coarser-resolution MODIS data was compared with fire-flagged area from the simultaneously acquired finer-resolution Advanced Thermal Emission and Reflection Radiometer (ASTER) data as a form of accuracy assessment. To date, no studies have examined the impact of spatial scaling on hyperspectral temperature retrieval.

With regards to vegetation, Nelson et al. (2009) coarsened both Landsat TM and ETM+ imagery to facilitate forest boundary detection, but found that different thresholds must be set depending on the spatial resolution to avoid under- and over-detection of a boundary. Rahman et al. (2003) used spatial upscaling—or coarsening of spatial resolution—to determine the best spatial resolution needed to study properties of grassland and chaparral using AVIRIS data. Schaaf et al. (in press) combined spatial scaling and MESMA to map vegetation in the Uintah Mountain Range, Utah, USA, across three spatial resolutions of AVIRIS hyperspectral data: 20.0 m, 40.0 m, and 60.0 m. This study found that the results of the MESMA modeling of vegetation did not vary drastically across the spatial resolutions (reported accuracies were 87.6% at 20.0 m, 86.1% at 40.0 m, and 83.3% at 60.0 m, each resulting from when the endmembers selected from the 20 m data were used). Similar spatial scaling analysis for fire detection and temperature modeling using hyperspectral data may provide valuable information for the development of future coarser spatial resolution hyperspectral sensors like HyspIRI.

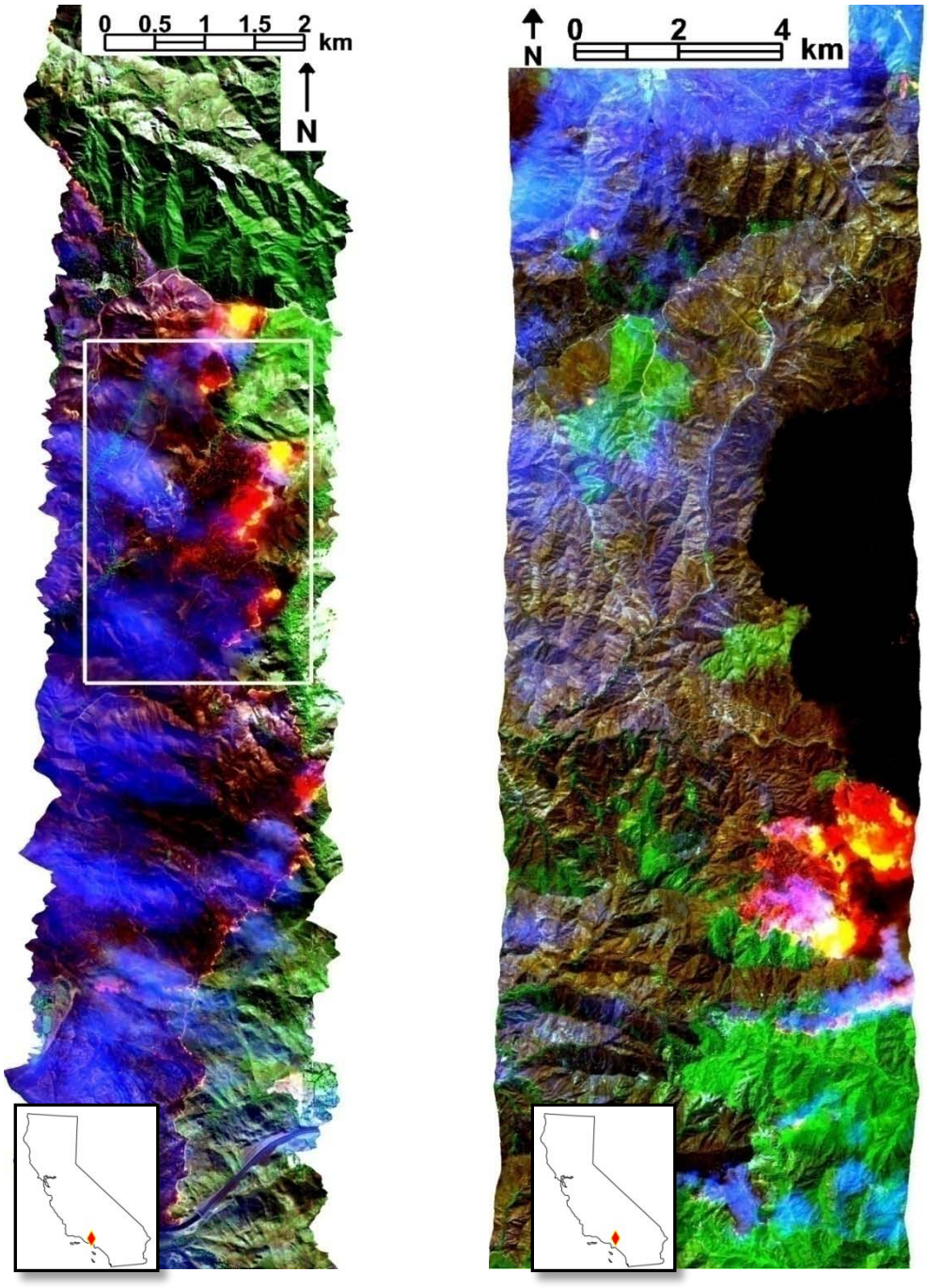

Figure 1. False color composites of the 2003 Simi (left) and 2009 Station (right) Fires. Both composites use bands centered at 1.7 µm (red), 1.1 µm (green), and 0.66 µm (blue). The Simi composite contains a white border of the subset used for the Gaussian data and subsequent comparison.

3 METHODS

3.1 Image Data

The AVIRIS sensor has an instantaneous field of view of 1 milliradian, which produces varying spatial resolutions in acquired data depending on the height of the platform. Each of the four AVIRIS scenes used in this research was acquired from one of two aerial platforms: an ER-2 used for high altitude missions, or a Twin Otter that flies at lower altitudes and acquires finer spatial resolution images. Data for all fires were delivered as radiometrically calibrated products, with geometric correction and geographic referencing provided by an onboard global positioning system and inertial data (Boardman, 1999). A SWIR-NIR-red composite of each fire scene is shown in Figs. 1 and 2.

At approximately 21:05 UTC on October 27, 2003, the AVIRIS sensor onboard a NASA Twin Otter platform collected data over the Simi Fire in the Santa Susana Mountains north of Los Angeles, California, USA. The Simi Fire burned a total of 438 km^2 from its start on October 25 to November 5, 2003. The platform averaged a 5.6 km altitude over the flight line, producing a 4.0 m spatial resolution in the AVIRIS image.

The Zaca Fire burned nearly 1,000 km^2 from July 4, 2007 to September 2, 2007 in the San Rafael Mountains in Santa Barbara County, California, USA, making it one of the largest and most expensive fires in California history (California Department of Forestry and Fire Protection, 2007). The AVIRIS sensor onboard a Twin Otter platform acquired data over a portion of the active fire area at approximately 15:00 UTC on

August 12, 2007. The average altitude of the platform during data acquisition for this flight line was 5.6 km, producing an image spatial resolution of 3.8 m.

In June 2008, the Indians Fire burned approximately 300 km^2 of the Santa Lucia Mountains along the central coast of California, USA. AVIRIS data were acquired from an ER-2 platform on June 11, 2008 at approximately 20:50 UTC. The average altitude of the platform during image acquisition was 19 km, producing a spatial resolution of 16.1 m for the AVIRIS scene.

The 2009 Station Fire burned 650 km^2 from August 16 to October 16, 2009 in the San Gabriel Mountains in Los Angeles County, California, USA. On August 31, 2009, data were gathered for the then full extent of the fire area by AVIRIS onboard an ER-2 platform. The majority of the active fire was covered in four flight lines, with a varying spatial resolution ranging between 10.0 and 12.0 m. The imagery from run 10 was selected for this study because it contained a large portion of the actively burning fire and was minimally covered by a large pyrocumulus cloud present over other portions of the active fire. The average altitude of the platform during acquisition of this image was 14.2 km, producing a spatial resolution of 10.7 m.

The center wavelengths and full-width half-maxima of AVIRIS bands change over time as the sensor is upgraded, so bands were subset independently for each AVIRIS scene. Spectra from each scene were visually examined to determine which bands contained water vapor absorption or scattering from smoke. Bands with wavelengths shorter than 1.2 μm contained degradation from smoke scattering (Dennison et al., 2006), and other bands centered near atmospheric water vapor absorption features were rejected.

A total of 95 NIR and SWIR bands were used for modeling the Zaca, Indians and Station Fire scenes, and 96 bands were used for modeling the Simi Fire scene.

To test the effects of spatial scaling on fire detection and temperature modeling, each of the fire images was resampled using pixel aggregation. The images were resampled by a doubling resample factor until a target spatial resolution close to 60.0 m was reached (Table 1). The resample factor was not doubled after the 42.8 m resolution of the Station Fire, since an 85.6 m resolution was beyond the proposed resolution of HyspIRI. Instead, the 10.7 m Station data was resampled by a factor of six, producing an image with a spatial resolution of 64.2 m. By maintaining a whole-number resampling factor, the aggregating of spectra from finer-resolution pixels into each coarser-resolution pixel was controlled for each fire. A saturation mask was used during the resampling to prevent saturated spectra from being averaged with nonsaturated spectra of other nearby pixels. The saturation mask assigned null values to bands with saturated spectra, thus keeping the resampled pixels from being spectrally distorted.

The pixel aggregate method gives equal weighting to all of the original pixels as they are averaged into coarser resolution pixels during resampling. The radiance within a single 64 m pixel created from 256 original 4.0 m pixels would be the mean of the radiance values of the 256 original pixels. However, the pixel aggregate method does not provide an accurate approximation of the point spread function of a coarser resolution sensor. A more realistic point spread function for a sensor with a ~60.0 m spatial resolution would more heavily weight the radiance reflected from or emitted by the center of the instantaneous field of view. For this reason, a Gaussian point spread function resampling method was used on a subset of the Simi Fire image. A 25 by 25

pixel kernel was generated with a full width half maximum (FWHM) of 15 pixels (60.0 m), the proposed spatial resolution of HyspIRI VSWIR. The kernel was applied to the 4.0 m image using a convolution filter, and the resulting image was then resampled to 60.0 m. The pixel aggregate resampling method was also used to resample the original 4.0 m saturation-masked subset by a factor of 15 to a 60.0 m spatial resolution, so that the impacts of the two spatial resampling methods could be directly compared.

The radiance values of the two 60.0 m images were compared at four AVIRIS channels (Fig. 3). As wavelength increased, more zero values were observed for the Gaussian resampled data which corresponded with nonzero values in the pixel aggregate data. These zero values resulted from the saturation mask being applied to a larger area (25 x 25 pixels) for the Gaussian resampled image. When the masked pixels are excluded, radiance values were strongly correlated at all four wavelengths (Fig. 3). The strongest correlation occurred at 597 nm, with an R^2 of 0.9987. The weakest correlation occurred in the SWIR at 1603 nm, with an R^2 of 0.9879, and a RMSE of 0.2539 $\mu Wcm^{-2}sr^{-1}nm^{-1}$. RMSE values did increase for the three wavelengths beyond the visible range, but the highest RMSE value (0.2748 $\mu Wcm^{-2}sr^{-1}nm^{-1}$) was found at 1098 nm. The lowest RMSE was 0.0552 $\mu Wcm^{-2}sr^{-1}nm^{-1}$, and occurred in the visible range at 597 nm.

3.2 Modeling

This research closely followed the fire temperature modeling methods used in Dennison and Matheson (2011), with some adjustments due to the spatial scaling. The HFDI was used to flag pixels likely to contain fire (Dennison and Roberts, 2009). HFDI is a ratio of two SWIR bands centered around 2.43 µm and 2.06 µm:

$$\text{HFDI} = \frac{(L_{2.43\mu m} - L_{2.06\mu m})}{(L_{2.43\mu m} + L_{2.06\mu m})} \quad (3)$$

Surfaces with elevated temperatures emit higher radiance at longer SWIR wavelengths relative to reflected solar radiance. HFDI will increase when fire is present within a pixel, allowing discrimination of pixels containing emitted radiance from fire. The index produces values ranging from -1 to 1, with high positive values indicating a greater likelihood of fire in a pixel, and lower values indicating a lesser likelihood of fire in a pixel. The threshold for fire detection is dependent on solar zenith angle and atmospheric water vapor concentration (Dennison and Roberts, 2009), so an appropriate threshold must be selected by the user. HFDI was calculated for each AVIRIS scene and at each spatial resolution using the bands with center wavelengths closest to 2.06 and 2.43 μm. The following threshold values were empirically selected for the four fire scenes: 0.00 (Simi), -0.15 (Zaca), 0.00 (Indians), and -0.10 (Station).

Pixels with HFDI values below these thresholds were modeled using a two-endmember linear spectral mixing models to map background land cover. This model has the form:

$$L_\lambda = f_{bg} L_{\lambda bg} + f_s L_{\lambda s} + \varepsilon_\lambda \quad (4)$$

where L_λ is the radiance measured by the sensor at each wavelength, L_{bg} is the radiance of the background endmember at that wavelength, $L_{\lambda s}$ is the radiance of the shade endmember accounting for atmospheric scattering, f_{bg} and f_s are the fractions of each endmember which sum to 1, and ε_λ is the residual error. The sum of the residual errors for all wavelengths was used to calculate root mean square error (RMSE). All unsaturated

pixels with HFDI values exceeding the indicated thresholds were modeled with a three-endmember linear spectral mixing model to retrieve fire temperature:

$$L_\lambda = f_{em}L_{\lambda em} + f_{bg}L_{\lambda bg} + f_s L_{\lambda s} + \varepsilon_\lambda \quad (5)$$

where $L_{\lambda em}$ is the radiance of the emitted radiance endmember at wavelength λ, and f_{em} is its associated fraction.

The emitted radiance and shade endmembers were modeled using the radiative transfer modeling software MODTRAN (Berk et al., 1989), while the background endmembers were acquired from each of the four finest spatial resolution AVIRIS scenes. The same modeled emitted and shade endmembers were applied to each resolution of each fire scene. The background endmembers acquired from the finest resolution image were also applied to the coarser resolutions, in order to isolate the effects of changing spatial resolution on fire detection and temperature modeling.

To create the emitted radiance spectral libraries, a total of 101 blackbody endmembers were modeled for each fire scene for temperatures ranging from 500 – 1500 K at 10 K intervals. Temperatures lower than 500 K were not used because Dennison et al. (2006) and Dennison and Roberts (2009) observed that the limited radiance that did exist in the SWIR for these cooler fire temperatures was unreliable for fire detection and temperature modeling.

A mid-latitude summer atmospheric model was used for each of the scenes. Image visibility for all images was set to 23 km, which is an overestimate of the visibility within the smoky portions of the scenes, but which accurately approximated the scattered solar radiance of dark objects in the less smoky portions of the scenes. A 5 km visibility

was tested for the Indians Fire scene, but showed no change in the emitted radiance endmembers at wavelengths used in the MESMA modeling (Dennison and Matheson, 2011). ACORN (ImSpec LLC) reflectance retrieval software was used to produce an average atmospheric water vapor concentration in areas near the fire of each scene. The water vapor values for each fire were: 493 atm-cm for the Indians Fire, 864 atm-cm for the Simi Fire, 898 atm-cm for the Zaca Fire, and 1069 atm-cm for the Station Fire. Emitted radiance spectra produced by MODTRAN were convolved to AVIRIS bands using band centers and FWHM for each dataset.

Like the emitted radiance endmembers, the shade endmembers were modeled for each fire scene using MODTRAN. This endmember contains only modeled atmospheric scattering, without emitted or reflected radiance (Eckmann et al., 2008). Each of the generated shade endmembers was convolved to AVIRIS band centers and FWHM.

Background radiance endmembers were used to account for reflected solar radiance. Similar to Dennison and Matheson (2011), separate libraries were generated for smoky and nonsmoky portions of the image to avoid misclassification due to smoke. During the MESMA modeling, pixels were classified into one of three categories: those containing smoke, those likely to contain fire, or those containing neither smoke nor fire. A smoke mask was generated for the original spatial resolution of each fire scene using a maximum likelihood classification. The masks were spatially resampled to the coarser resolutions using pixel aggregate resampling, which rounded averaged mask values to the nearest whole number for smoke or nonsmoke classification. For the subset of the Simi Fire scene with the Gaussian point spread function applied, the original 4 m smoke mask was resampled to 60.0 m using nearest neighbor resampling.

The background endmembers were selected from collected spectra for six land cover classes from each original finest resolution image. All of the scenes were acquired over mountainous areas in either central or southern California, areas which share some broad vegetation characteristics. For example, dense and sparse stands of chaparral and other shrubs are common in the region, taller stands of oak forest are located in riparian areas and north-facing slopes, and grasses are found in disturbed areas (Dennison et al., 2006). Other nonvegetation land cover types used for background modeling included soil and rock features, grouped into the same class, and ash. In the Indians Fire scene, a second class of ash was created to prevent over-modeling of grass in the smoke portion of the image. This over-modeling of grass in earlier model runs was likely because many of the ash spectra in the clearly burned smoke portion of the image contained absorption features similar to ligno-cellulose absorption features in the SWIR, characteristic of nonphotosynthetic vegetation like senesced grass (Dennison and Matheson, 2011).

An iterative endmember selection algorithm (Schaaf et al., in press) was used to find the reduced set of background endmembers that was still able to accurately classify the selected background spectra. Kappa coefficient (Cohen, 1960) was used to assess the accuracy of background spectrum classification. The iterative endmember selection algorithm was run until the kappa coefficient reached a minimum of 0.895, or until the improvement in kappa gained by adding additional endmembers reached a threshold of 0.0025. The final selected endmembers were then divided into the three categories; smoke, nonsmoke, and fire, with some overlap between the nonsmoke and fire categories. The fire category endmembers used for modeling fire-flagged pixels included soil/rock

and ash endmembers from smoky portions of the image, which were also included in the library to be used to model smoke-flagged pixels.

The number of selected background endmembers, along with their associated kappa coefficients, is summarized for each fire in Table 2. For all fires, the endmembers were divided into three broad vegetation classes (grass, chaparral/shrubland, and oak/riparian forest) and at least two nonvegetation classes (ash and soil/rock). The fire endmember libraries for each scene consisted of the nonvegetated smoke endmembers, with the exception of the Station Fire. Due to varying concentrations of smoke in the within that scene, all 26 endmembers were used in the smoke library, and 21 of the 26 endmembers were used in the nonsmoke library.

3.3 Multiple Endmember Spectral Mixture Analysis

Each radiance image, paired with a smoke mask and an HFDI mask, was modeled using MESMA. If a pixel had an HFDI value higher than the HFDI threshold, it was modeled with three endmembers: an emitted radiance endmember, a shade endmember, and a background endmember from the fire library. If a pixel had an HFDI value lower than the threshold, it was modeled with two endmembers: a shade endmember, and a background endmember from the smoke library if the smoke mask flagged that pixel, or a background endmember from the nonsmoke library if no smoke was present.

The model used singular-value decomposition to fit all possible combinations of endmembers from the appropriate libraries in order to solve for the endmember fractions that best modeled each pixel spectrum. Saturated bands were removed from modeling using the saturation radiance value for each band, and pixels were required to have two or

more nonsaturated bands for modeling. Endmember fractions were constrained to between 0 and 1. The model producing the lowest RMSE was assigned to each pixel.

Modeled temperature and fire fractional areas were compared between all the resolutions of each fire scene. Modeled temperatures were summed by fire fractional area to calculate the area modeled at each temperature at each spatial resolution. The Kolmogorov-Smirnov (K-S) statistic, a nonparametric test (Massey, 1951), was used to compare the histograms of area modeled at each temperature across the range of spatial resolutions. A *p*-value threshold of 0.05 was used, with values lower than this indicating a failure to reject a null hypothesis of no difference between two temperature area distributions. Total area of fire detection was directly compared between all spatial resolutions using the Lee-Sallee shape index (Lee and Sallee, 1970). This index is generated by dividing the intersecting area between the two shapes of modeled fire area by the union of the two areas. Values range from 0 to 1, where 0 indicates no agreement and 1 indicates total agreement.

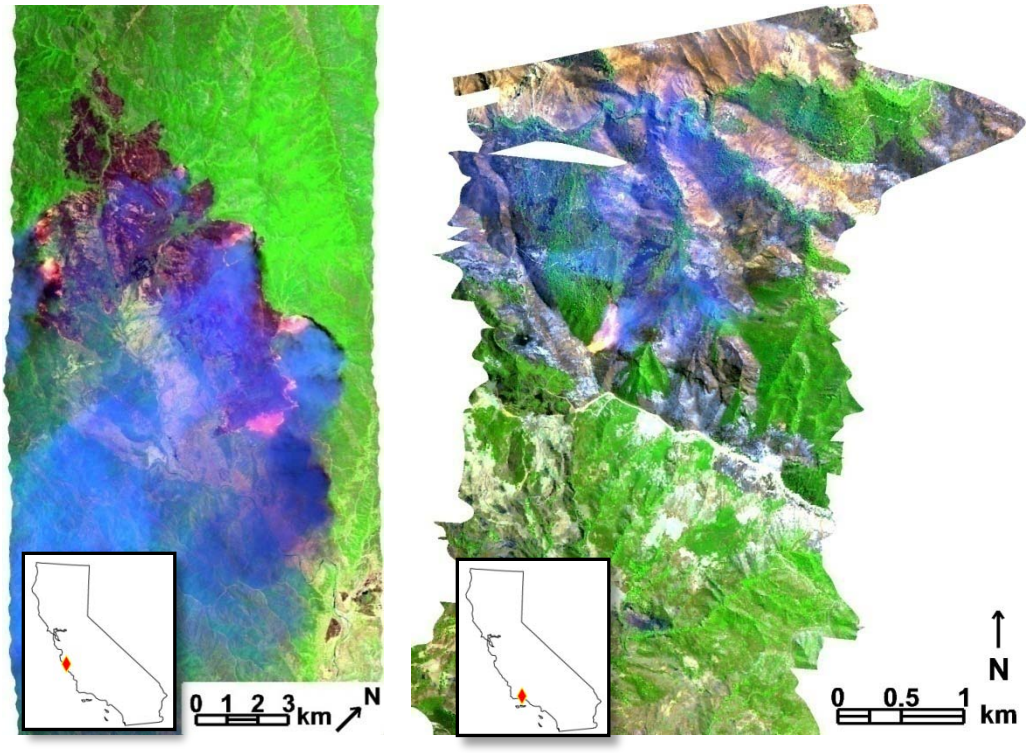

Figure 2. False color composites of the 2008 Indians (left) and 2007 Zaca (right) Fires. Both composites use bands centered at 1.7 µm (red), 1.1 µm (green), and 0.66 µm (blue).

Table 1. Spatial information of the four original fire scenes and their coarsened resolutions.

Fire	Simi	Zaca	Indians	Station
Platform	Twin Otter	Twin Otter	ER-2	ER-2
Platform Altitude (km)	5.6	5.6	19.0	14.2
Original Resolution (m)	4.0	3.8	16.1	10.7
Resampled resolutions (m)	8.0, 16.0, 32.0, 64.0	7.6, 15.2, 30.4, 60.8	32.2, 64.4	21.4, 42.8, 64.2

Table 2. Summary of the background endmembers and their respective kappa coefficients selected for all resolutions of each fire.

Fire	**Total Background Endmembers**	**K**	**Non smoke**	**Smoke**	**Fire**	**Veg. Classes**	**Nonveg. Classes**
Simi	37	0.896	19	18	8	3	2
Indians	63	0.801	34	29	14	3	3
Zaca	23	0.899	14	9	5	4	2
Station	26	0.899	26	21	5	3	2

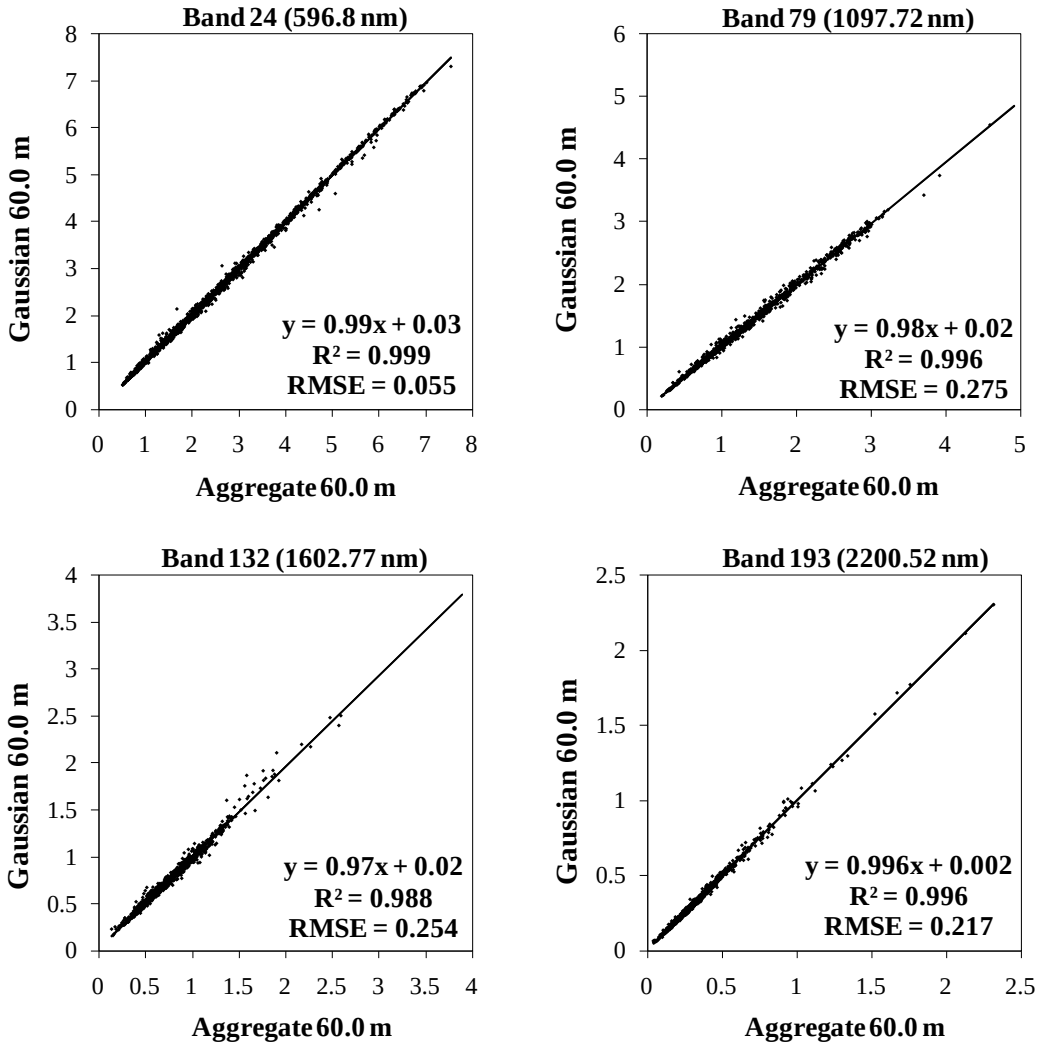

Figure 3. Scatterplots comparing radiance values (in $\mu Wcm^{-2}sr^{-1}nm^{-1}$) at four wavelengths of pixels from a subset of the Simi Fire using two different spatial resampling techniques.

4 RESULTS

Modeled temperatures (Fig. 4) and fire fractional area (Fig. 5) were visually compared for the all resolutions of the Simi Fire scene. For visualization purposes, a subset of the modeled temperatures and fire fractional area is displayed, including the 60 m resolution subsets comparing the two resampling methods (Figs. 4f-g and 5f-g). Fig. 4 illustrates very similar trends in temperature distribution across all spatial resolutions. The majority of the fire was modeled with temperatures between 500 and 1000 K, with the hottest temperatures modeled in pixels along the fire front. Results were similar to Dennison et al. (2006), who found that the majority of pixels were modeled with temperatures above 750 K. Cooler temperatures were found in areas ahead of the fire front, due to scattering of emitted radiance coming from the hot-burning fire front (Dennison and Matheson 2011). Along the fire front, fewer high-temperature pixels were modeled at coarser resolution. This was likely due to saturation masking during resampling. There is a large hotspot along the fire front where temperatures appear to cool down as the spatial resolution coarsens. The saturated center of this hotspot grows larger in area as spatial resolution coarsens. As spatial resolution coarsened, fewer isolated low-temperature pixels were modeled behind the fire front.

The 60.0 m Gaussian resampled image (Fig. 4g) contains a few additional pixels modeled with fire temperature compared to the 60.0 m pixel aggregate resampled image (Fig 4f). Most of the additional pixels in the Gaussian resampled image were modeled with low fire temperatures. Notably, the Gaussian resampled image had fewer modeled

pixels along the fire front due to the saturation masking procedure. The Gaussian resampled image had 64 pixels masked as saturated, twice as many pixels masked in the aggregate resampled image.

Similarly, spatial distributions of fire fractional areas appeared to remain consistent across multiple spatial resolutions (Fig. 5). In general, the highest fire fractional areas were modeled along the fire front. In the areas ahead of the fire front where cooler temperatures were modeled, corresponding fire fractional areas were also low. Again, larger saturation areas were left unmodeled at coarser resolutions. As spatial resolution coarsened to 64 m, fire fractional area greatly increased in areas behind the fire front. The few pixels modeled in the Gaussian resampled data that were not modeled in the aggregate resampled data possessed low fire fractions. Higher fire fractional areas appeared to be more spread out in Fig. 5g compared to Fig. 5f.

The modeled temperature and fire fractional area for the full fire extent of the Simi Fire and for the other fire scenes are provided in Figs. 6 – 13. Results for the other fires displayed similar patterns across coarsening spatial resolution as the Simi Fire. Highest temperatures and fire fractions were found in areas along the fronts of fires, although with coarsening spatial resolution, fire fractional area increased in areas behind the fire. Low temperatures with low fire fractional area were modeled over nonfire pixels located ahead of the fire fronts, with the exception of the Zaca Fire, where an apparent nonfire portion of the subset near the fire hot spot was modeled with low temperatures (Fig. 11), but with high fire fractional area (Fig. 12). This area could have contained subcanopy ground fires. Temperatures gradually cooled and varied less with coarsening spatial resolution, while fire fractional area gradually increased. The number of small,

isolated hotspots with modeled burning temperatures also decreased with decreasing spatial resolution.

By multiplying the dimensions of each pixel by its fire fractional area, total area modeled at each temperature was calculated and compared with HFDI-flagged area for each fire scene (Table 3). In all cases, a coarsening of spatial resolution corresponded with an increased fire area. HFDI flagged far more area for fire, since area was assessed based on entire pixels, rather than fire fractional area. The trend for the Zaca, Indians and Station Fires was that the coarsest resolution modeled approximately 1.5 times the original resolution's total modeled fire area. However, the Simi Fire 64 m data modeled more than three times the total fire area of the 4.0 m data. HFDI detected fire in a higher number of pixels and larger area for the Simi data than for the other scenes, both for the original resolution (211,212 pixels or 3,379,392 m^2) and for each subsequent resampling (e.g., 1215 pixels or 4,976,640 m^2 at 64.0 m). While the difference in HFDI area between the finest and the coarsest resolutions of a fire scene was also greatest for the Simi Fire (a 47% increase in flagged area from 4.0 m to 64.0 m data), the difference was not as great as the total modeled fire area for the Simi Fire (a 172% increase in modeled area from 4.0 m to 64.0 m). For the Simi Fire 60.0 m resampling comparison, both HFDI and the temperature modeling calculated slightly more area for the Gaussian resampled data than for the aggregate data.

The histograms of total fire area for each temperature were plotted on a logarithmic scale to highlight differences across a wide range of area (Figs. 14 – 18). All histograms exhibit the broad trend of decreasing area with increasing fire temperature, regardless of spatial resolution. Area modeled between 500 K and approximately 850 K

increased with coarsening resolution for the Simi Fire (Fig. 14). It is clear that increase in area modeled at coarser spatial resolutions (Table 3) is coming from this temperature range. This trend reverses from 850 to approximately 1150 K, with finer spatial resolutions exhibiting higher modeled area. Only the two finest resolutions, 4.0 m and 8.0 m, modeled area for the hottest temperatures from approximately 1400 to 1500 K. The highest temperatures modeled for the three coarsest resolutions were 1410 K for 16 m, 1390 K for 32.0 m, and 1270 K for 64.0 m. The largest area was modeled for the lowest temperature (500 K) for all resolutions except for 32.0 m, which peaked at 570 K, and 64.0 m, which peaked at 740 K.

By plotting the total area modeled at each temperature for the two 60 m resampled subsets of the Simi Fire (Fig. 15), minor differences between the two resampling methods became clearer. The modeled area was similar between the two results across all temperatures, although the Gaussian data generally yielded more modeled area for temperatures between 500 and 800 K. The range with the largest area difference between the two resampling techniques was between 500 and 550 K. The results from the 60.0 m pixel aggregate resampled image produced its largest modeled area at 700 K, while the 60.0 m Gaussian resampled image had the largest modeled area at 540 K. For temperatures beyond 800 K, both resampling methods produced a comparable results, although the Gaussian resampled image had one pixel modeled at 1270 K, while the aggregate resampled image had a cooler maximum temperature of 1190 K.

Histograms for the five resolutions of the Zaca Fire (Fig. 16) demonstrate similar patterns to those of the Simi Fire, albeit on a smaller scale, since the fire captured in the scene was much smaller. For the range of temperatures from 500 to approximately 900 K,

greater area was generally modeled for coarser resolutions. Peak area was modeled at 520 K for all spatial resolutions except for 60.8 m, which peaked at 560 K. Area drops considerably for temperatures beyond 900 K for all spatial resolutions, but unlike the Simi Fire, coarser resolutions up to 30.4 m have a small area modeled at 1500 K. There is a gap in modeled temperature for all spatial resolutions between the range of 1340 and 1460 K. Coarser spatial resolutions have a larger gap; for example, the gap for 30.4 m data ranges from 1020 to 1490 K, while the gap for 3.8 m data only ranges between 1340 and 1490 K.

For the Indians Fire scene (Fig. 17), the three resolutions produced similar distributions for low temperatures between 500 and 600 K. The peak area modeled for all resolutions was at 550 K. Total area modeled at each temperature produced similar histograms for the Station Fire (Fig. 18). The Station Fire was larger, so more area was modeled for a wider range of temperatures. With the exception of the temperature range 510 – 680 K, area modeled for temperatures below 1050 K remained consistent across all spatial resolutions. All resolutions modeled the largest area at 500 K. 10.7 m and 21.4 m spatial resolutions produced reduced modeled area for 510 – 540 K, while coarser spatial resolutions modeled no area within this temperature range. For hotter temperatures, more area was generally modeled by the finer spatial resolutions.

The results from the Kolmogorov-Smirnov nonparametric tests between the temperature-area distributions at each spatial resolution are summarized in Table 4. For all of the fires, the distributions from the finest resolution data and from the coarsest resolution data were statistically different. With the exception of the Zaca Fire, all of the fire scenes display a trend where each resolution’s distribution could not be considered

statistically different from that of the next coarsest resolution. The Zaca Fire's distributions were statistically different between the 15.2 m and 30.4 m resolutions, and between the 30.4 m and 60.8 m resolutions. The small size of the Zaca Fire within the AVIRIS scene could have contributed to the significance differences between these spatial resolutions. For example, at 60.8 m, only 52 pixels in the scene were flagged as likely to contain fire by HFDI. Another exception to the overall trend occurred in the Station Fire scene, where the distributions for 21.4 m and 64.2 m could not be considered statistically different. The K-S test between the two 60.0 m subsets of the Simi Fire produced a *D*-statistic of 0.069 and a *p*-value of 0.963, indicating a high correlation between the histogram distributions.

Spatial agreement in fire detection area between different spatial resolutions, as assessed by the Lee-Sallee index, was consistently highest for the comparison of the finest resolution and the first resampled resolution (Table 5). Agreement was higher for closer spatial resolutions (e.g., 8.0 m and 16.0 m), and decreased for more widely separated spatial resolutions (e.g., 8 m and 32 m). Table 5 also shows a pattern of decreasing Lee-Sallee values between sequential resolutions as spatial resolution coarsened (e.g., values along the diagonal for each fire). Overall agreement was best between the 3.8 m and 7.6 m resolutions of the Zaca Fire, with a Lee-Sallee value of 0.909. Interestingly, the Zaca Fire also contained the pair of resolutions that produced the poorest agreement, a Lee-Sallee value of 0.669 between the 30.4 m and 60.8 m resolutions. Comparison between the two 60.0 m subsets of the Simi Fire produced a Lee-Sallee value of 0.832, indicating fair agreement.

Mean RMSE values were assessed for pixels modeled at four selected temperatures across all spatial resolutions of each fire scene (Table 6). Reference temperatures of 500, 700, 900, and 1100 K were selected, but two scenes (the Simi Fire 60.0 m subsets and the Zaca Fire) had poor representation at those temperatures so alternative temperatures were selected (Table 6). Where the coarsening factor was doubled from the previous resolution, the number of pixels modeled at each temperature decreased approximately by a factor of 2 as spatial resolution coarsened. Higher modeled temperatures produced higher mean RMSE values, but mean RMSE values also tended to decrease as spatial resolution coarsened. For the Simi subset, temperatures were selected for which both resampling methods modeled a comparable fire fractional area. Correspondingly, both methods modeled a similar number of pixels for each temperature. For all shown temperatures except for 1190 K, the pixel aggregate resampled data produced higher mean RMSE values than the Gaussian resampled data. Examination of residual spectral trends showed that residuals were largest near atmospheric water vapor absorption features, similar to trends observed by Dennison and Matheson (2011).

Background endmembers were modeled similarly across all spatial resolutions of all four fire scenes. An example is shown for the subset of the Simi Fire, including the two 60.0 m subsets comparing the two resampling methods (Fig. 11). Qualitatively, classifications across all spatial resolutions match up very well with land cover as it appears in the radiance images, although more and more detail was lost with coarsening spatial resolution. The saturated area in the fires (in red) can be seen growing larger with coarser spatial resolutions. More pixels were saturated in the Gaussian resampled image aggregate resampled image, although the saturated areas are spatially co-located. Minor

differences in the background classification occurred because of the difference in resampling methods. These differences consisted mostly of conflicts between soil/rock and ash, grass and soil/rock, and between the three vegetation classes. Background endmember modeling results for all of the scenes are shown in Fig. 19 – 23.

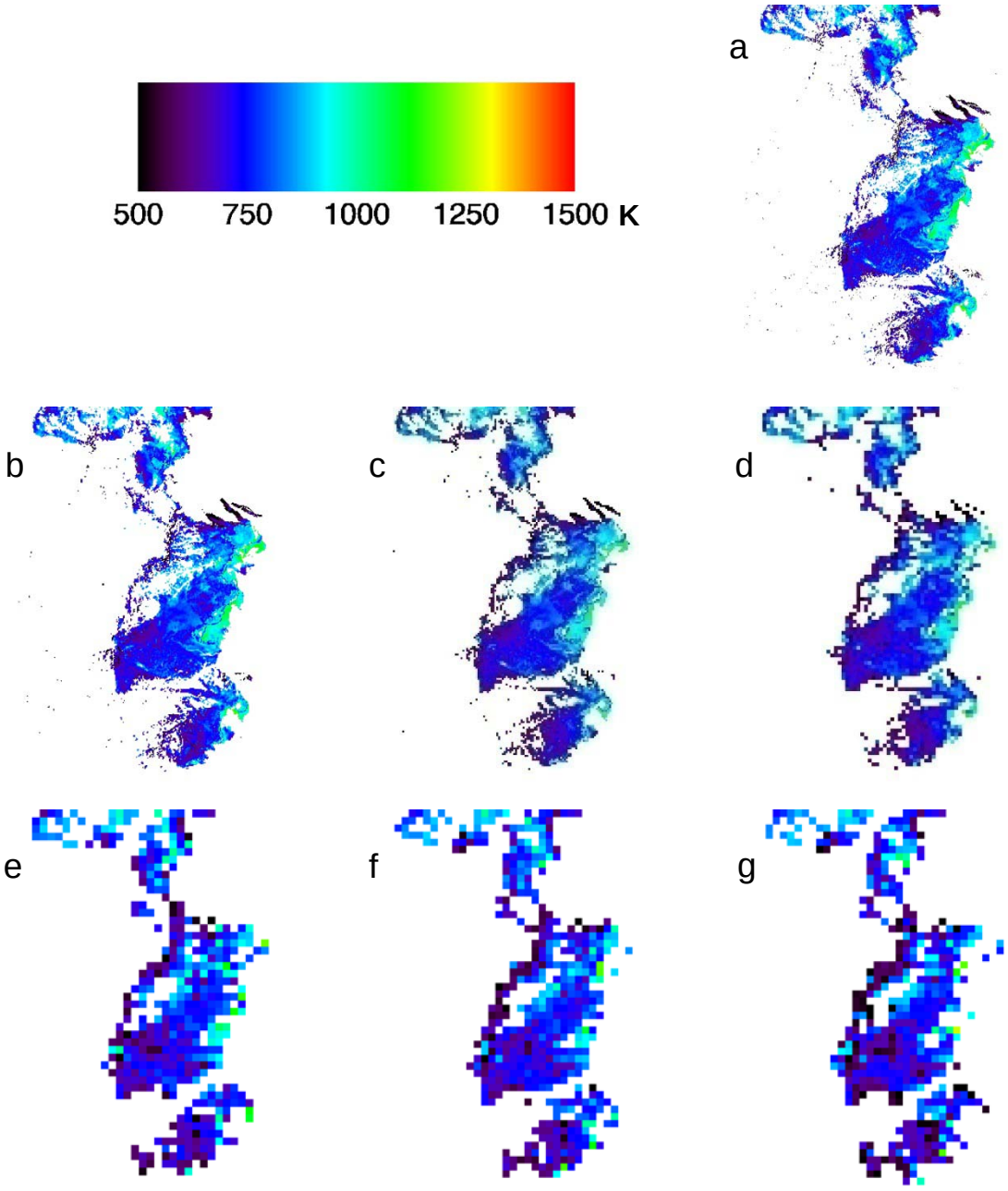

Figure 4. Modeled temperatures for a subset of the Simi Fire scene at spatial resolutions of 4.0 m (a), 8.0 m (b), 16.0 m (c), 32.0 m (d), 64.0 m (e), 60.0 m pixel aggregation resampled (f), and 60.0 m Gaussian resampled (g).

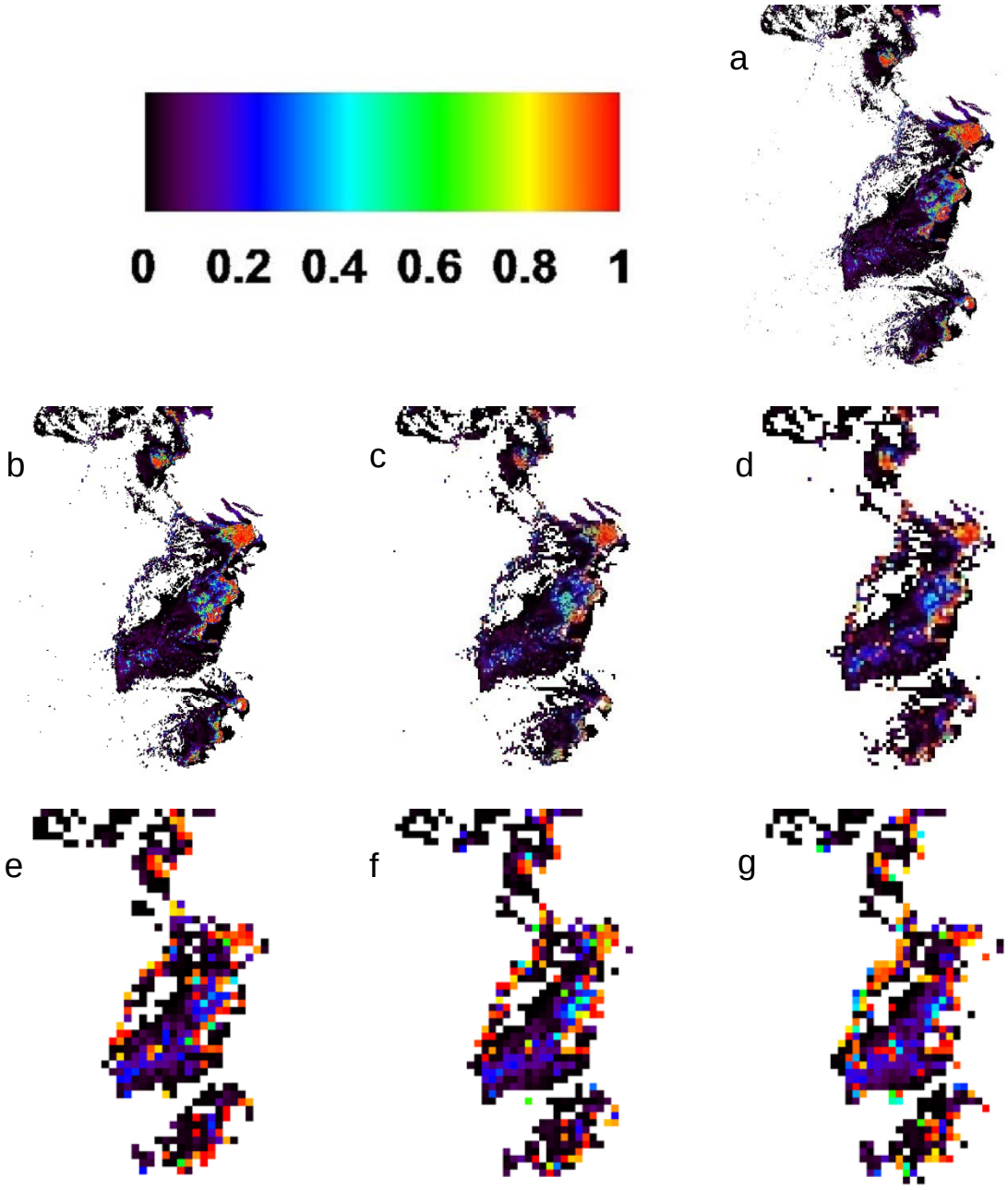

Figure 5. Modeled fire fractional area for a subset of the Simi Fire scene at spatial resolutions of 4.0 m (a), 8.0 m (b), 16.0 m (c), 32.0 m (d), 64.0 m (e), 60.0 m pixel aggregation resampled (f), and 60.0 m Gaussian resampled (g).

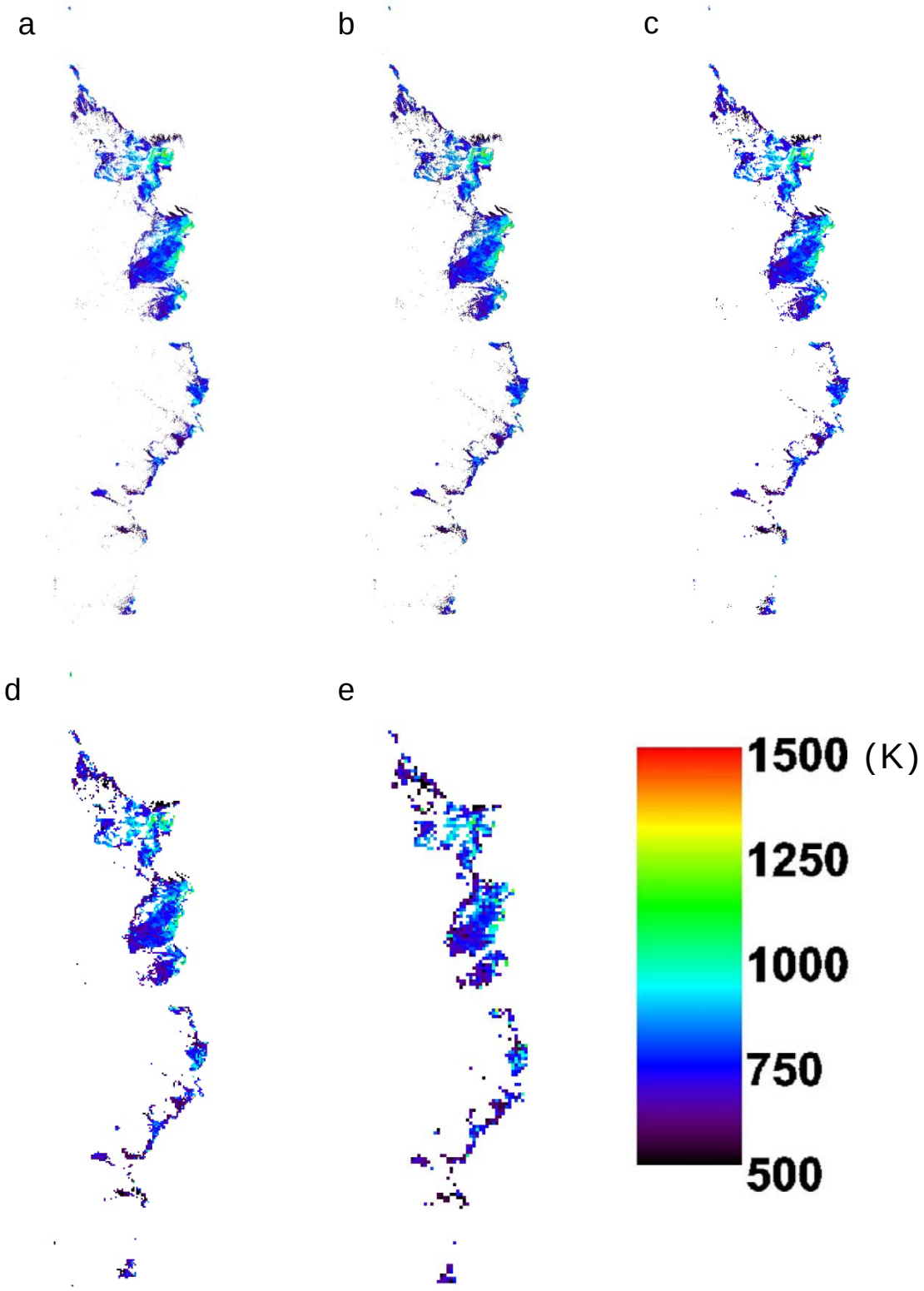

Figure 6. Modeled temperatures for the Simi Fire scene at spatial resolutions of 4.0 m (a), 8.0 m (b), 16.0 m (c), 32.0 m (d), and 64.0 m (e).

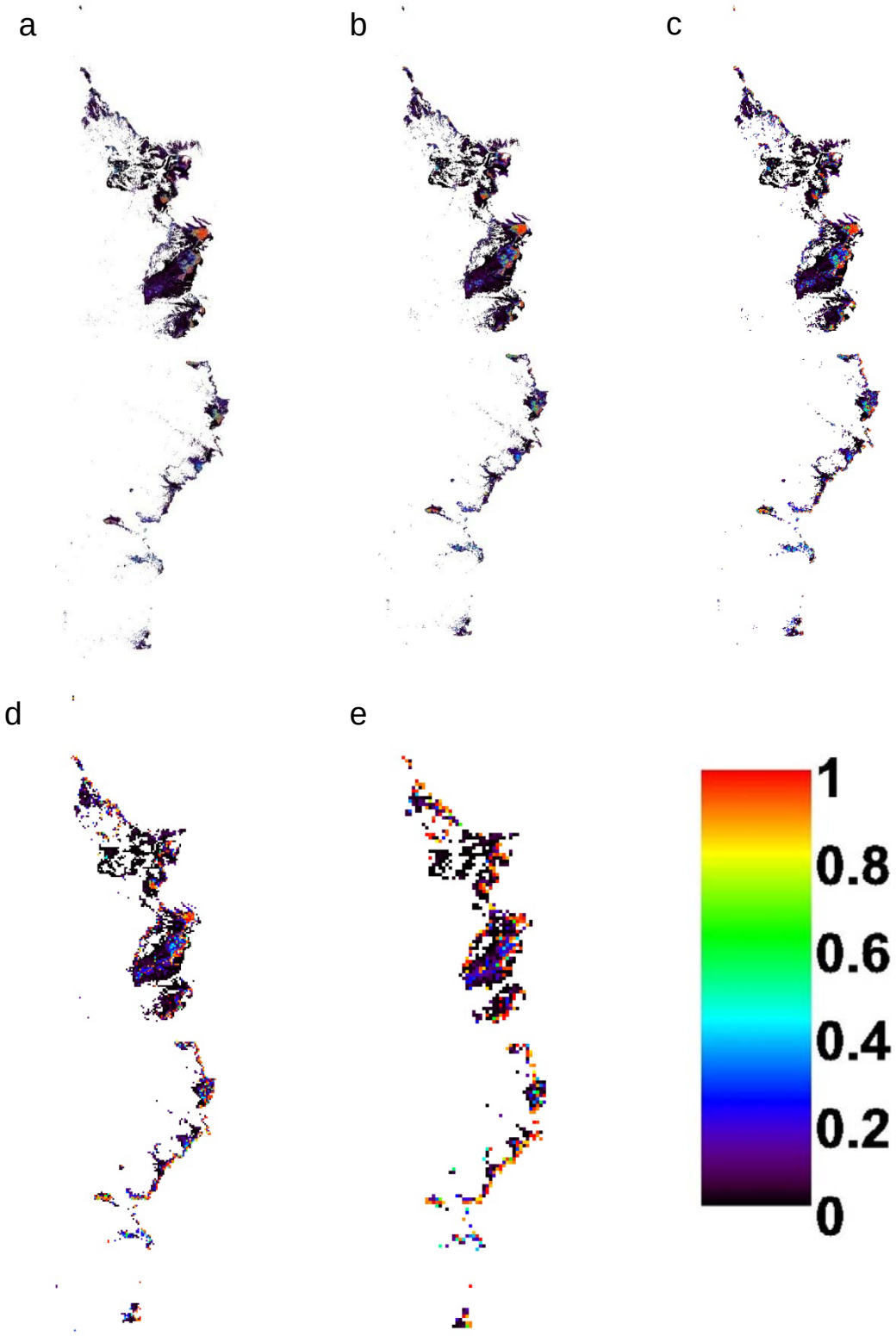

Figure 7. Modeled fire fractional area for the Simi Fire scene at spatial resolutions of 4.0 m (a), 8.0 m (b), 16.0 m (c), 32.0 m (d), and 64.0 m (e).

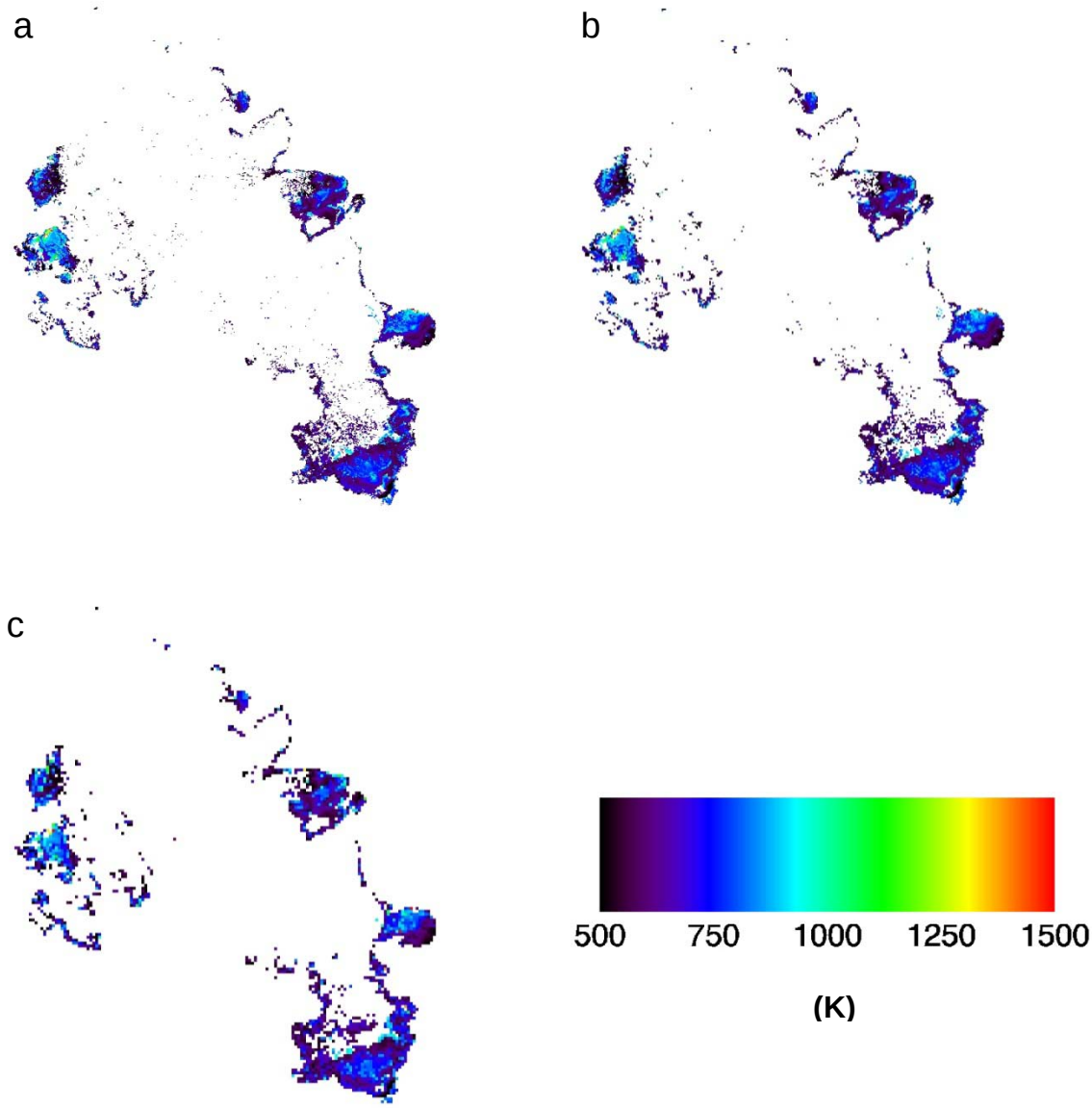

Figure 8. Modeled temperature for the Indians Fire scene at spatial resolutions of 16.1 m (a), 32.2 m (b), and 64.4 m (c).

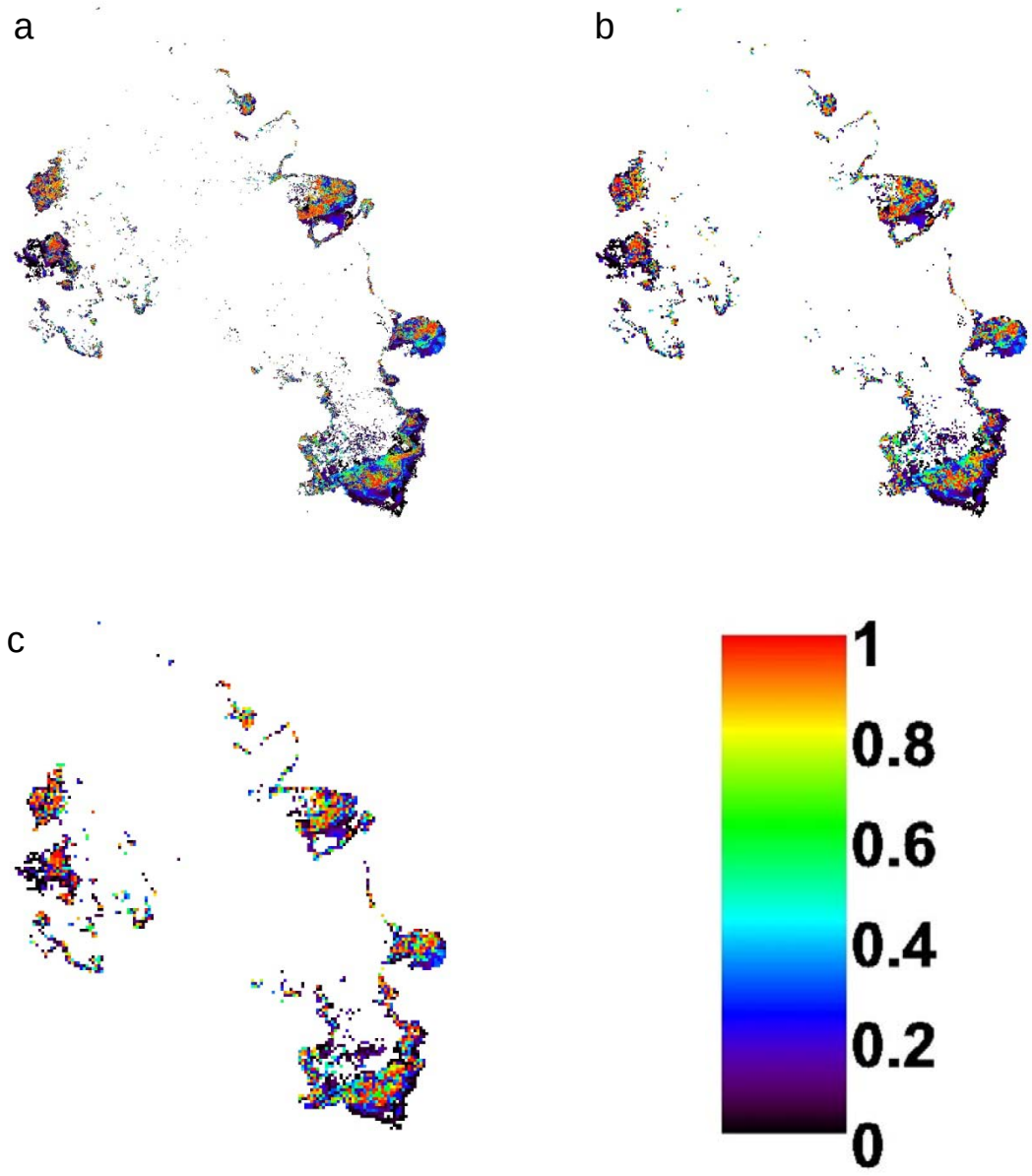

Figure 9. Modeled fire fractional area for the Indians Fire scene at spatial resolutions of 16.1 m (a), 32.2 m (b), and 64.4 m (c).

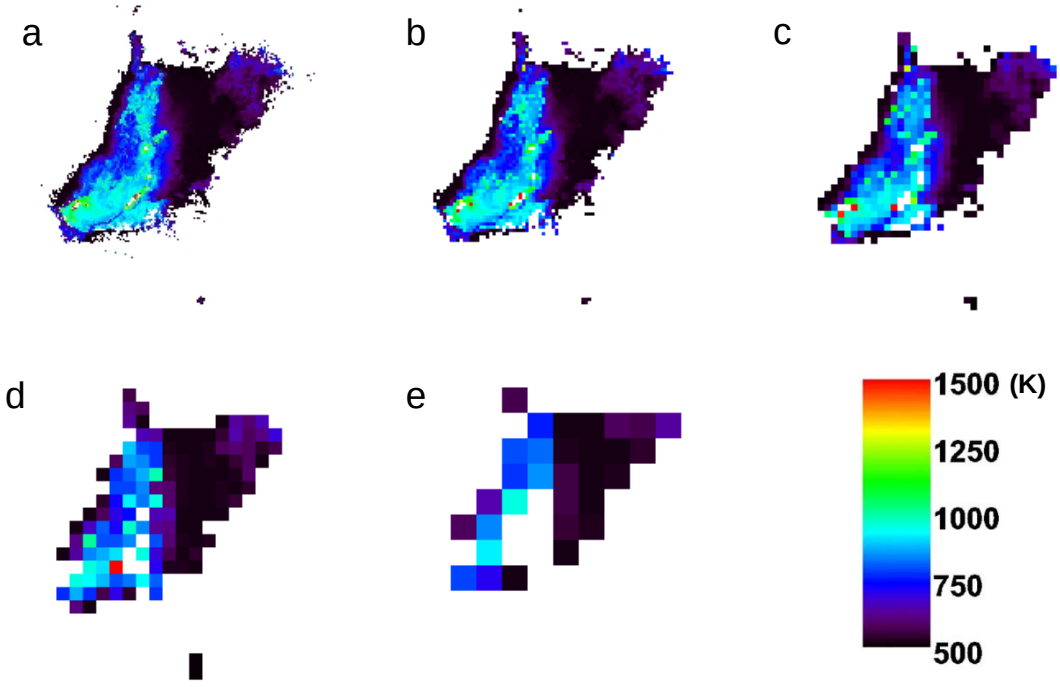

Figure 10. Modeled temperature for the Zaca Fire scene at spatial resolutions of 3.8 m (a), 7.6 m (b), 15.2 m (c), 30.4 m (d), and 60.8 m (e).

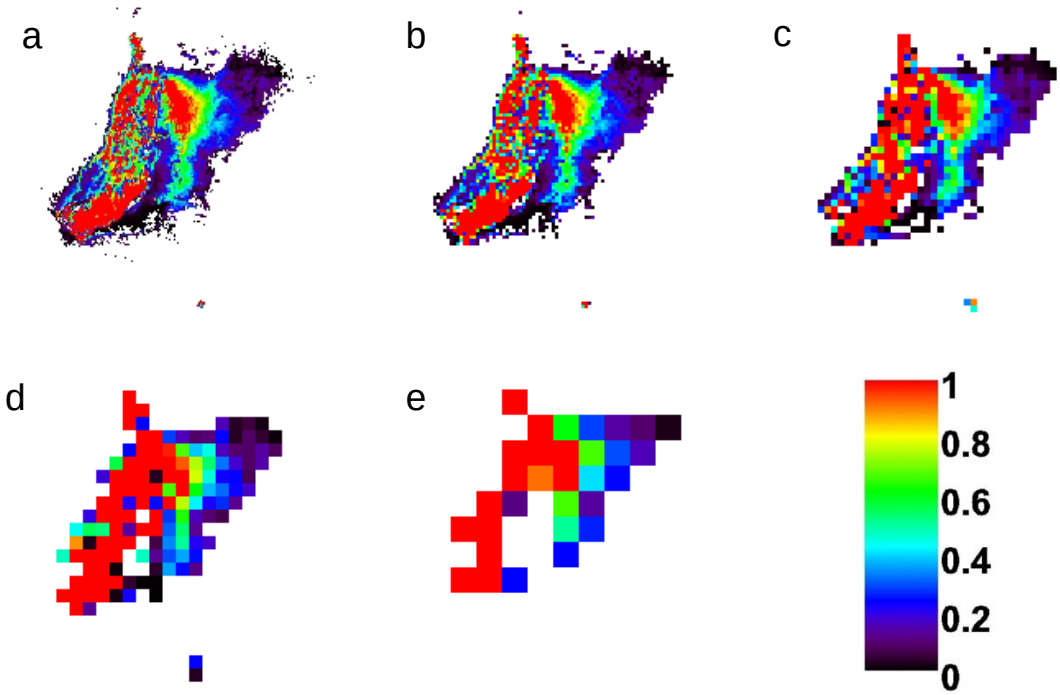

Figure 11. Modeled fire fractional area for the Zaca Fire scene at spatial resolutions of 3.8 m (a), 7.6 m (b), 15.2 m (c), 30.4 m (d), and 60.8 m (e).

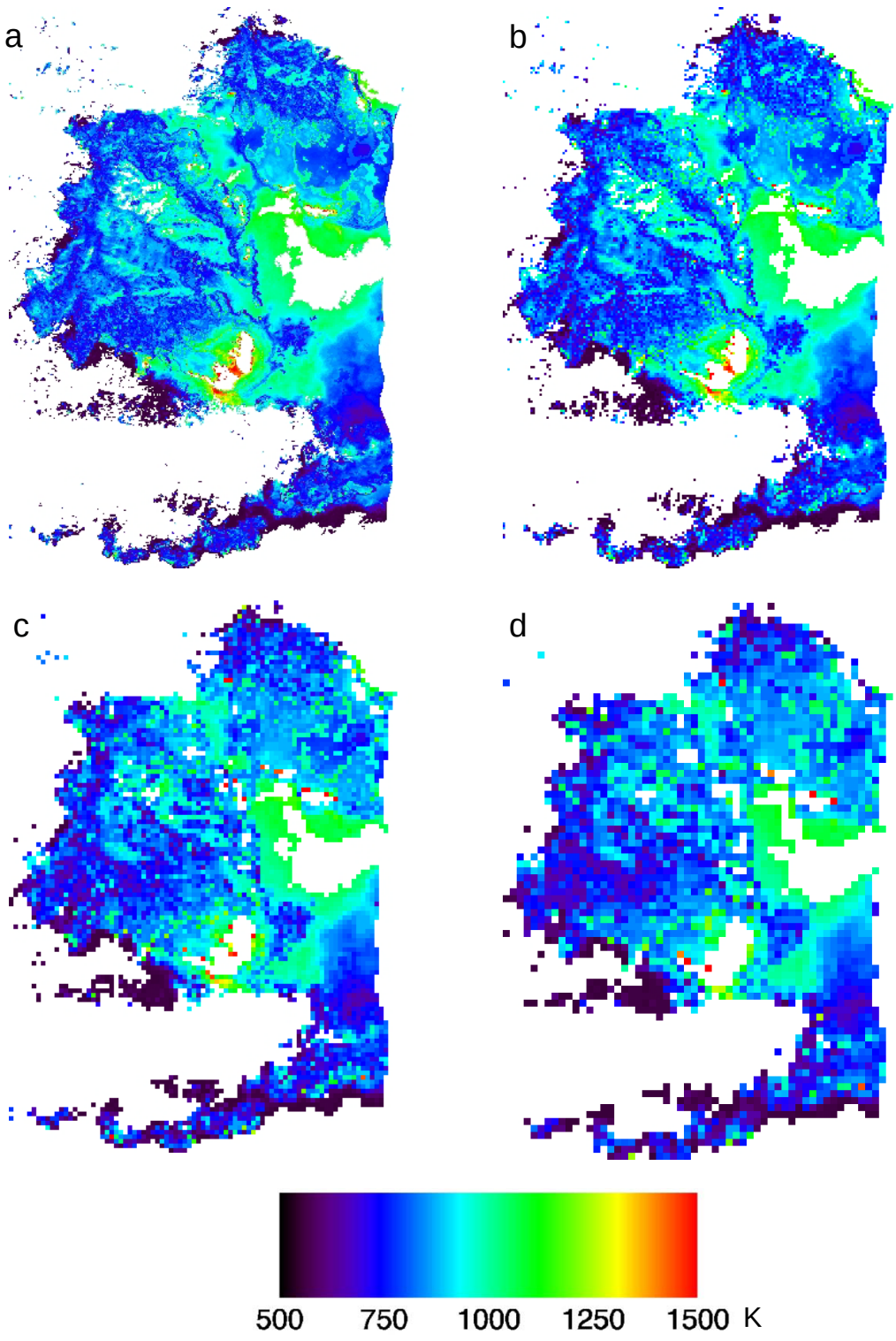

Figure 12. Modeled temperature for the Station Fire scene at spatial resolutions of 10.7 m (a), 21.4 m (b), 42.8 m (c), and 64.2 m (d).

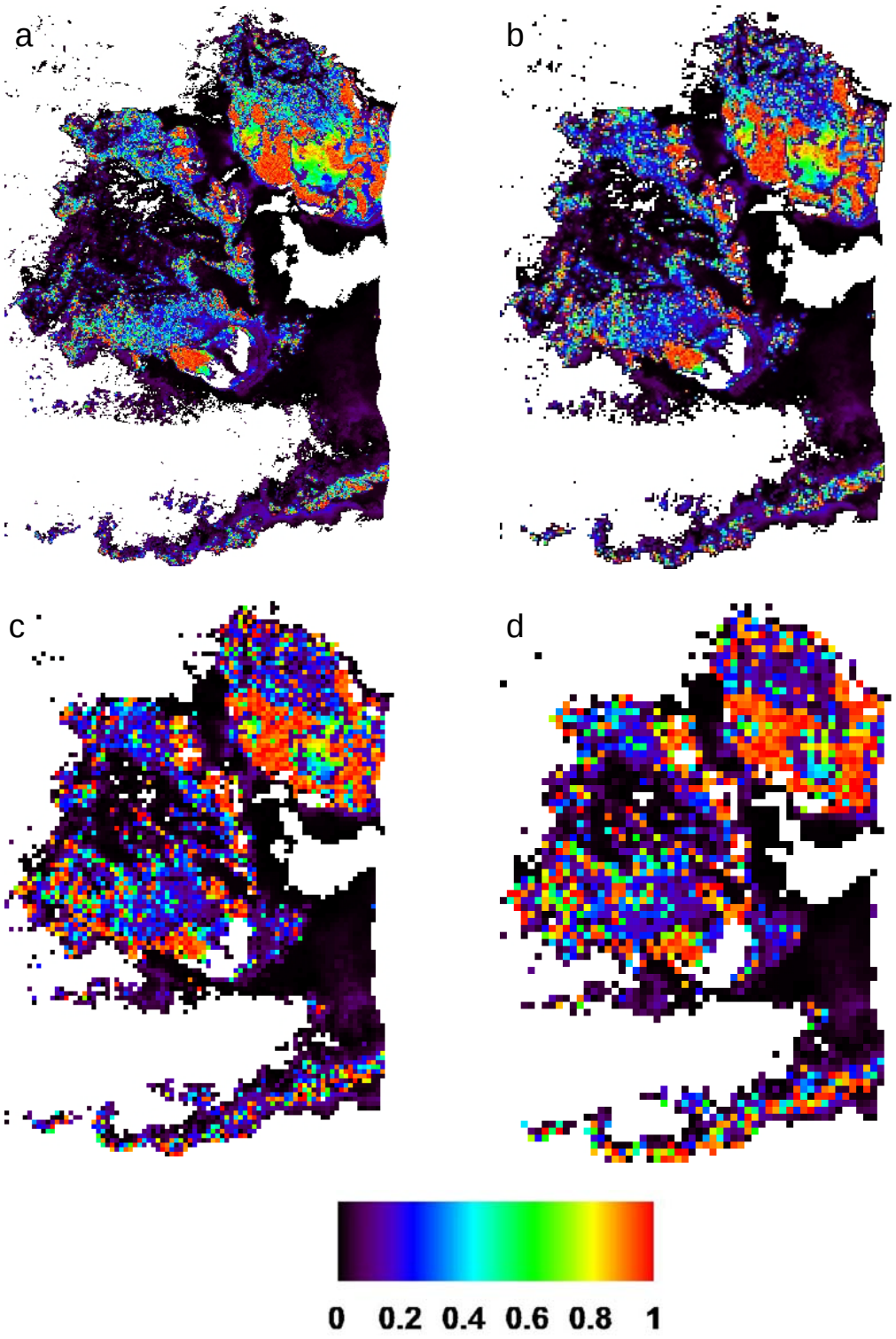

Figure 13. Modeled fire fractional area for the Station Fire scene at spatial resolutions of 10.7 m (a), 21.4 m (b), 42.8 m (c), and 64.2 m (d).

Table 3. Total modeled fire area for all spatial resolutions of each fire scene.

Resolution	Total HFDI-Flagged Area (m^2)	Total Modeled Fire Area (m^2)
SIMI		
64.0 m	4,976,640	1,022,406
32.0 m	4,154,368	656,209
16.0 m	3,720,448	475,394
8.0 m	3,471,616	405,503
4.0 m	3,379,392	376,365
SIMI RESAMPLING COMPARISON		
60.0 m Pixel Aggregate	2,138,400	383,645
60.0 m Gaussian	2,300,400	463,766
INDIANS		
64.4 m	10,837,052	3,499,755
32.2 m	10,125,779	3,146,770
16.1 m	9,745,259	2,896,847
ZACA		
60.8 m	192,225	59,789
30.4 m	177,439	58,162
15.2 m	169,583	47,069
7.6 m	168,890	41,154
3.8 m	169,901	39,202
STATION		
64.2 m	20,612,322	3,546,167
42.8 m	20,525,767	3,160,673
21.4 m	20,236,794	2,683,086
10.7 m	20,067,807	2,493,645

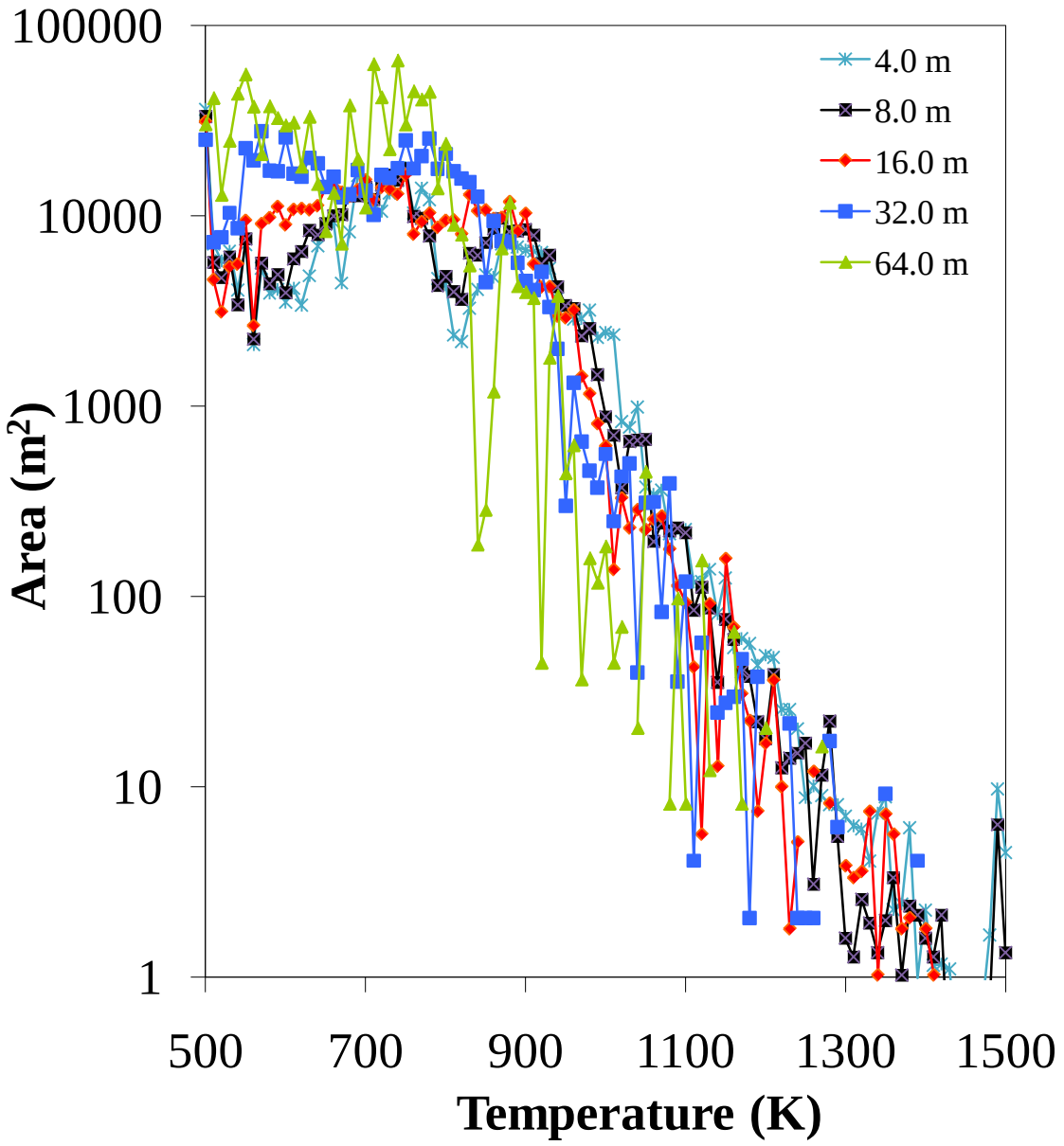

Figure 14. Histograms showing total area modeled at each temperature for all spatial resolutions of the Simi Fire. Temperatures for which no area was modeled are not shown, which produces “missing lines” between some individual points.

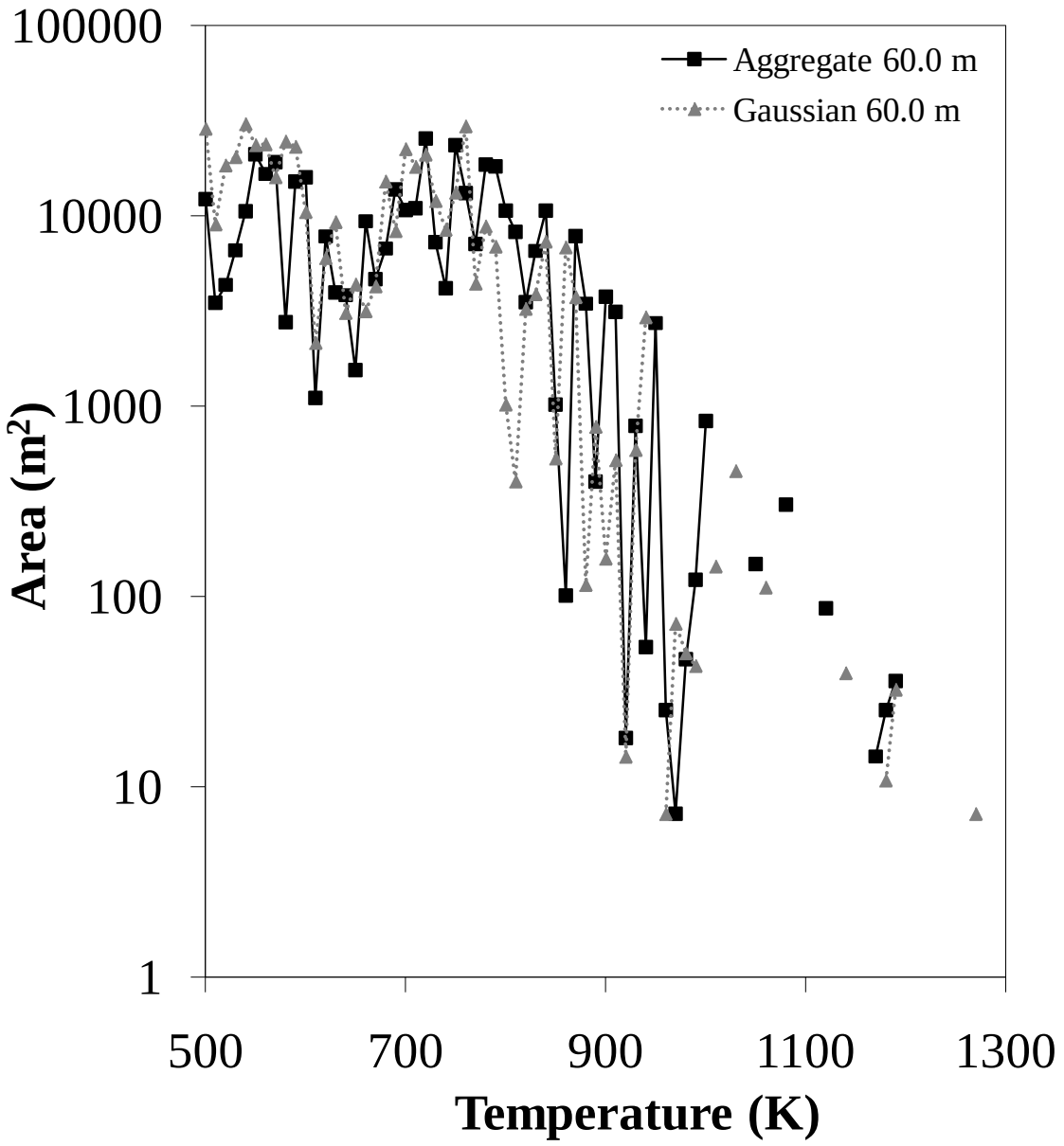

Figure 15. Histograms showing total area modeled at each temperature for a subset of the Simi Fire comparing two resampling methods at two spatial resolutions. Temperatures for which no area was modeled are not shown, which produces “missing lines” between some individual points.

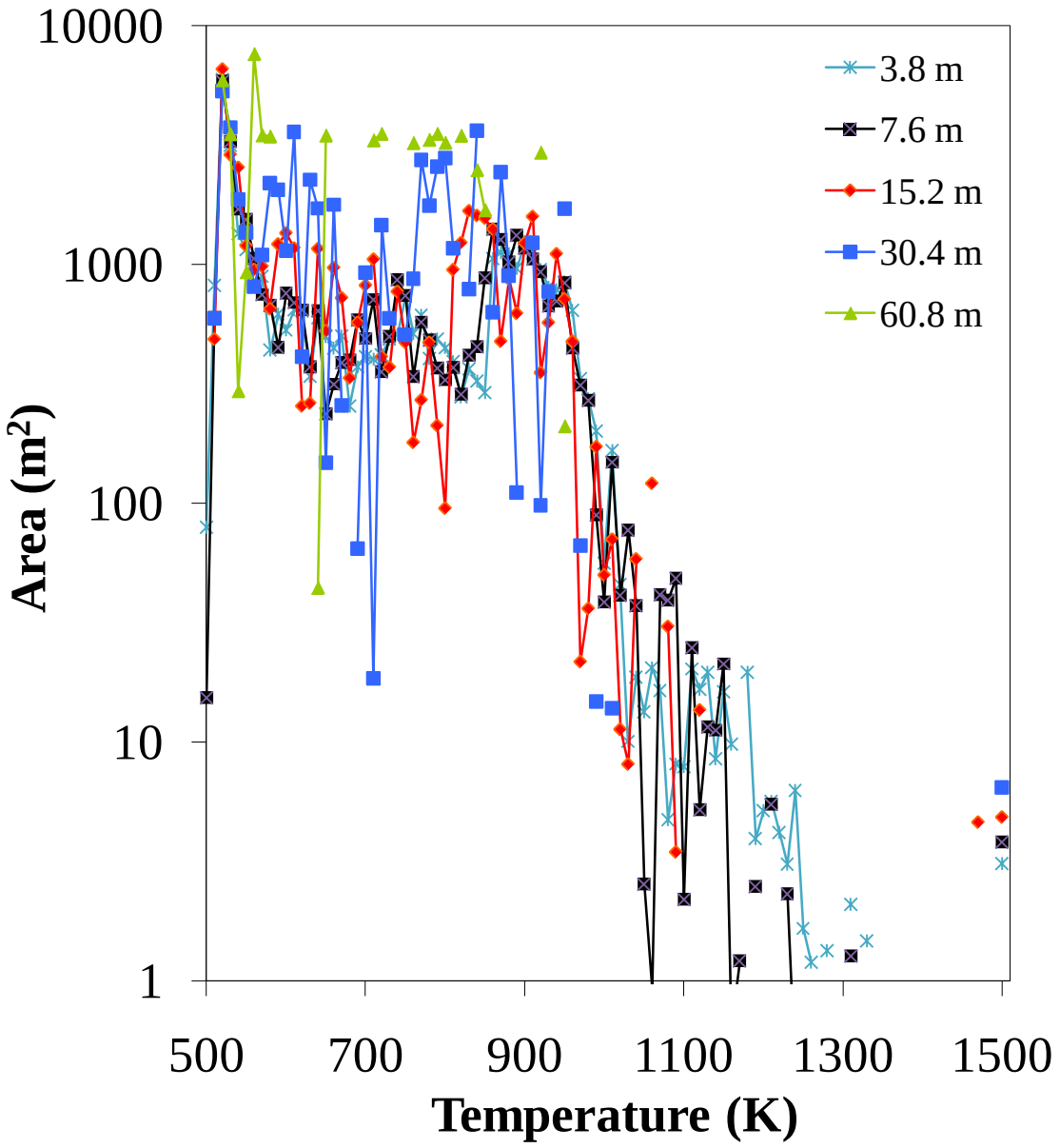

Figure 16. Histograms showing total area modeled at each temperature for all spatial resolutions of the Zaca Fire. Temperatures for which no area was modeled are not shown, which produces “missing lines” between some individual points.

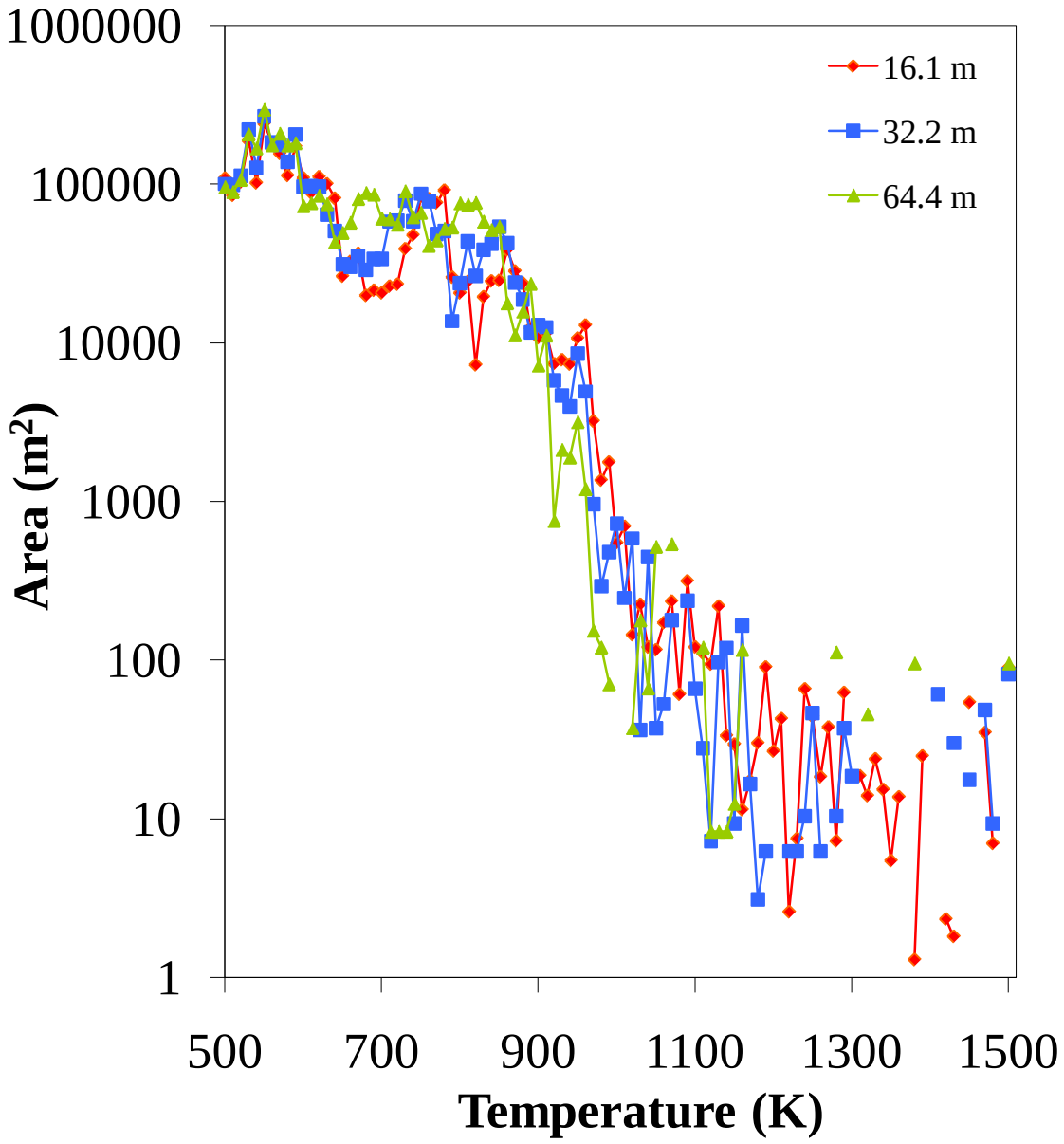

Figure 17. Histograms showing total area modeled at each temperature for all spatial resolutions of the Indians Fire. Temperatures for which no area was modeled are not shown, which produces “missing lines” between some individual points.

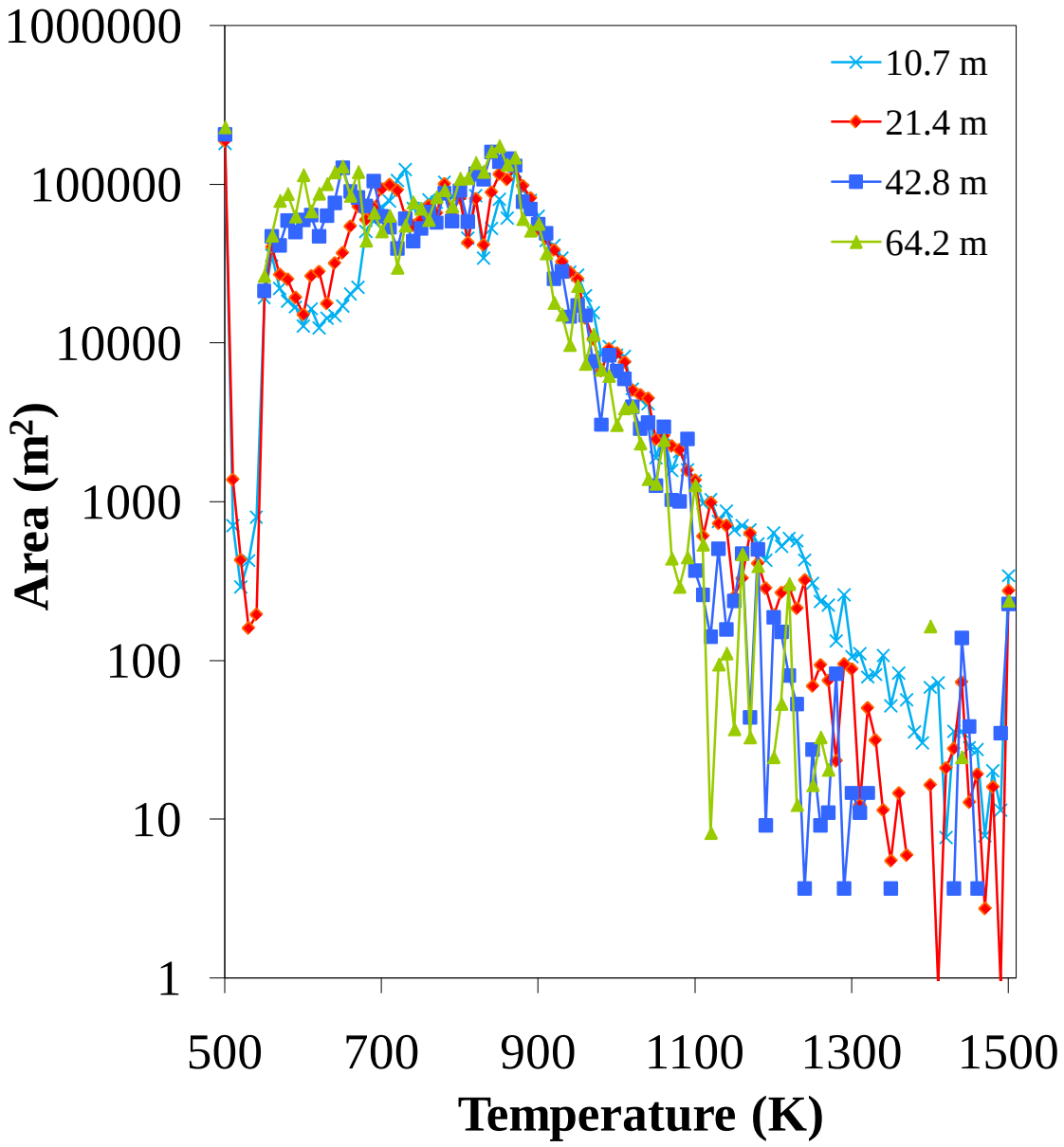

Figure 18. Histograms showing total area modeled at each temperature for all spatial resolutions of the Station Fire. Temperatures for which no area was modeled are not shown, which produces “missing lines” between some individual points.

Table 4. Kolmogorov-Smirnov statistics for comparisons of area modeled at each temperature for all spatial resolutions of the Simi, Indians, Zaca, and Station Fires. Shaded values have corresponding statistically significant *p*- values, indicating that the distributions are significantly different.

SIMI	4.0 m	8.0 m	16.0 m	32.0 m
8.0 m	0.1089			
16.0 m	0.2178	0.1782		
32.0 m	0.2376	0.2178	0.2277	
64.0 m	0.3663	0.3465	0.2574	0.1782

INDIANS	16.1 m	32.2 m
32.2 m	0.1262	
64.4 m	0.2816	0.1748

ZACA	3.8 m	7.6 m	15.2 m	30.4 m
7.6 m	0.0990			
15.2 m	0.2079	0.1287		
30.4 m	0.3960	0.3168	0.1881	
60.8 m	0.6238	0.5446	0.4158	0.2277

STATION	10.7 m	21.4 m	42.8 m
21.4m	0.1188		
42.8m	0.2277	0.1683	
64.2m	0.2772	0.2376	0.1089

Table 5. Lee-Sallee shape index results comparing the area of all pixels modeled with a fire fraction for all spatial resolutions of the Simi, Indians, Zaca, and Station Fires, respectively.

SIMI	8.0 m	16.0 m	32.0 m	64.0 m
4.0 m	0.853	0.767	0.676	0.570
8.0 m		0.815	0.707	0.591
16.0 m			0.768	0.627
32.0 m				0.701

INDIANS	32.2 m	64.4 m
16.1 m	0.806	0.706
32.2 m		0.761

ZACA	7.6 m	15.2 m	30.4 m	60.8 m
3.8 m	0.909	0.851	0.750	0.606
7.6 m		0.885	0.770	0.610
15.2 m			0.810	0.634
30.4 m				0.669

STATION	21.4 m	42.8 m	64.2 m
10.7 m	0.828	0.744	0.701
21.4 m		0.797	0.739
42.8 m			0.788

Table 6. Mean RMSE values (in $\mu Wcm^{-2}sr^{-1}nm^{-1}$) for pixels modeled with specific temperatures at all resolutions of each fire scene.

	SIMI							
	500 K		700 K		900 K		1100 K	
Spatial Resolution	Pixels	Mean RMSE	Pixels	Mean RMSE	Pixels	Mean RMSE	Pixels	Mean RMSE
4.0 m	9,696	0.0339	7,270	0.2025	2,877	0.2837	371	0.4390
8.0 m	2,342	0.0329	1,928	0.1750	763	0.2857	113	0.3499
16.0 m	595	0.0327	514	0.1469	206	0.2487	23	0.3033
32.0 m	126	0.0342	120	0.1149	46	0.1749	9	0.1923
64.0 m	29	0.0332	29	0.0603	8	0.0692	1	0.0543
	SIMI Subset							
	550 K		720 K		930 K		1190 K	
	Pixels	Mean RMSE	Pixels	Mean RMSE	Pixels	Mean RMSE	Pixels	Mean RMSE
60.0 m Gaussian	9	0.0466	25	0.0577	7	0.0482	1	0.0004
60.0 m Aggregate	8	0.0501	18	0.1174	6	0.0957	1	0.0004
	STATION							
	500 K		700 K		900 K		1100 K	
	Pixels	Mean RMSE	Pixels	Mean RMSE	Pixels	Mean RMSE	Pixels	Mean RMSE
10.7 m	16,565	0.0273	2,270	0.2374	1,747	0.3754	241	0.4869
21.4 m	4,178	0.0273	639	0.2275	380	0.3366	57	0.4850
42.8 m	1,134	0.0272	147	0.1672	115	0.2877	10	0.2321
64.2 m	561	0.0270	51	0.1717	31	0.3525	12	0.2414
	INDIANS							
	500 K		700 K		900 K		1110 K	
	Pixels	Mean RMSE	Pixels	Mean RMSE	Pixels	Mean RMSE	Pixels	Mean RMSE
16.1 m	1,142	0.0751	617	0.2543	192	0.5604	19	0.7975
32.2 m	269	0.0781	153	0.2049	49	0.5738	5	0.3296
64.4 m	74	0.0706	58	0.1610	13	0.2945	1	0.2043
	ZACA							
	520 K		710 K		950 K			
	Pixels	Mean RMSE	Pixels	Mean RMSE	Pixels	Mean RMSE		
3.8 m	2,133	0.1309	133	0.3635	106	0.9434		
7.6 m	532	0.1291	37	0.3239	31	0.8249		
15.2 m	150	0.1202	11	0.2065	8	0.6266		
30.4 m	35	0.1205	1	0.0724	4	0.7196		
60.8 m	9	0.1062	1	0.0267	1	0.1288		

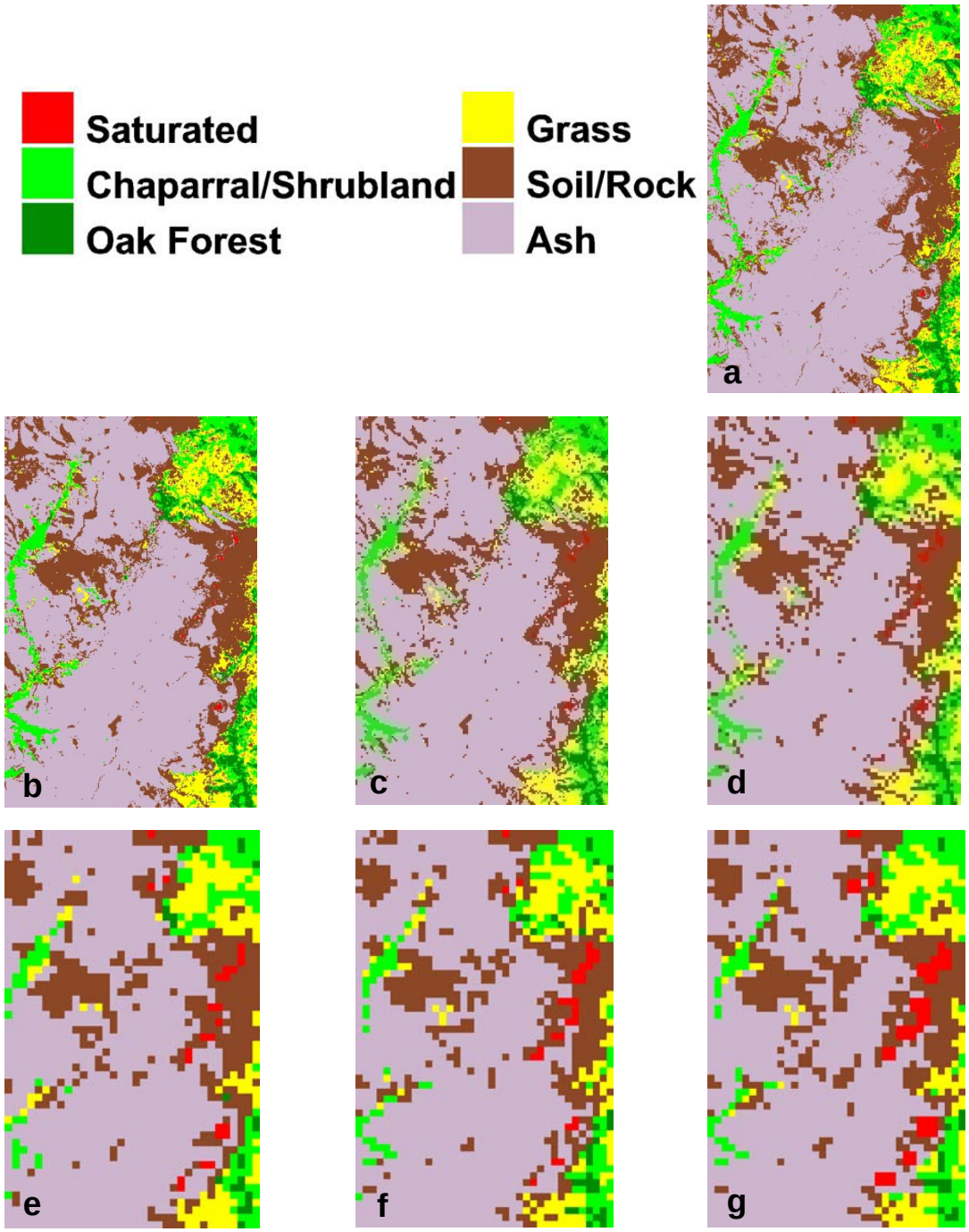

Figure 19. Background endmembers mapped from the Simi Fire scene at spatial resolutions of 4.0 m (a), 8.0 m (b), 16.0 m (c), 32.0 m (d), 64.0 m (e), 60.0 m pixel aggregate resampled (f), and 60.0 m Gaussian resampled (g).

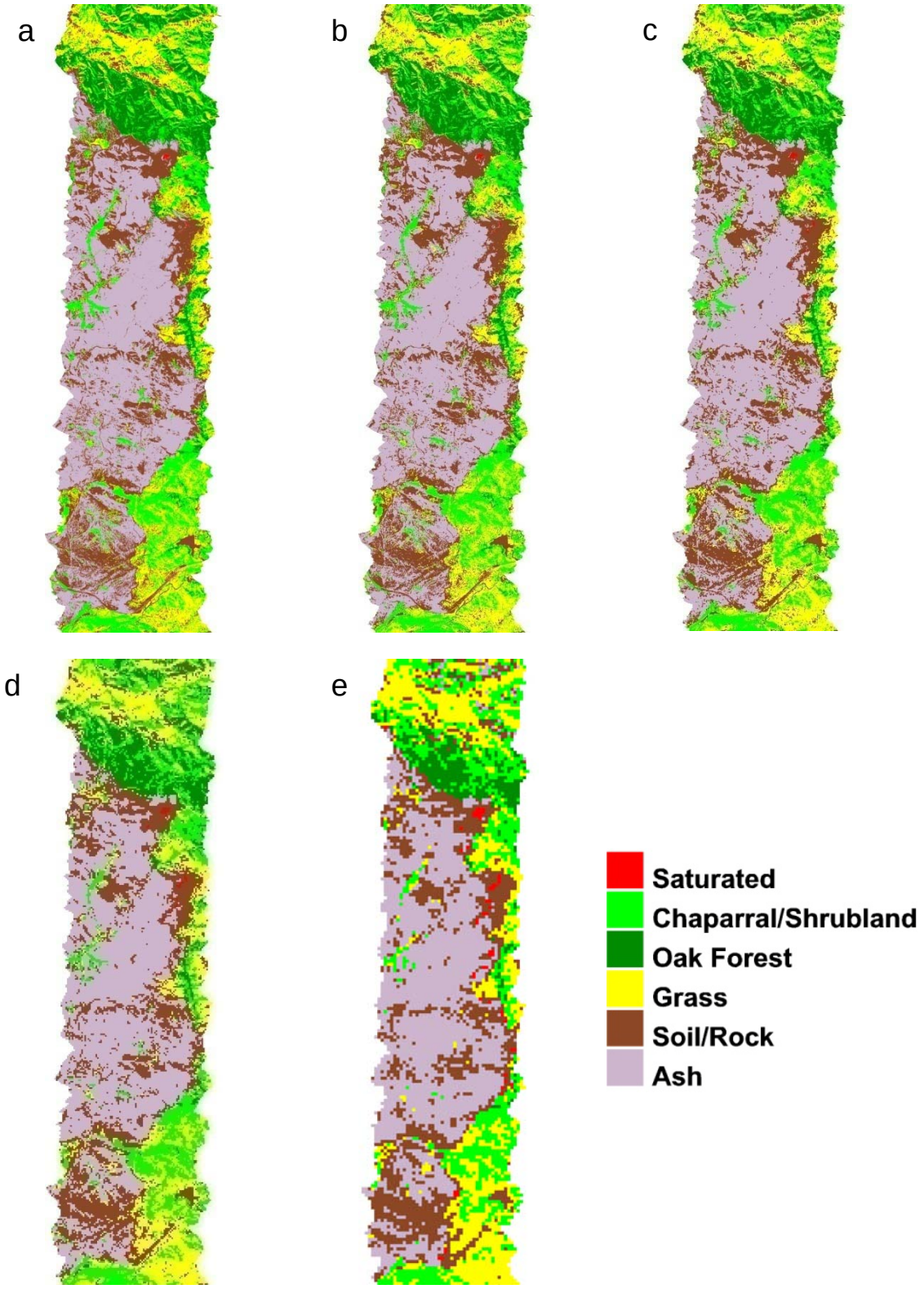

Figure 20. Background endmembers mapped for the Simi Fire scene at spatial resolutions of 4.0 m (a), 8.0 m (b), 16.0 m (c), 32.0 m (d), and 64.0 m (e).

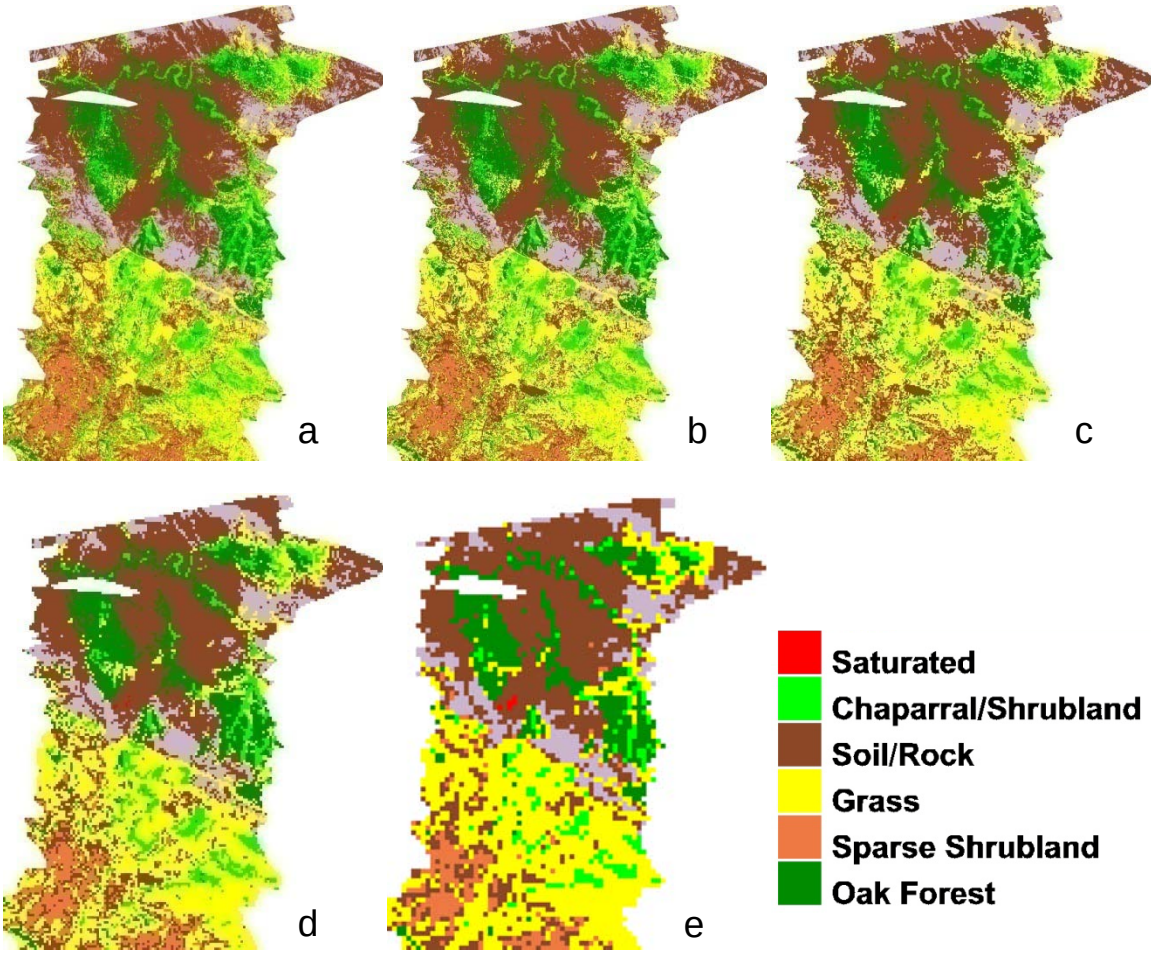

Figure 21. Background endmembers mapped for the Zaca Fire scene at spatial resolutions of 3.8 m (a), 7.6 m (b), 15.2 m (c), 30.4 m (d), and 60.8 m (e).

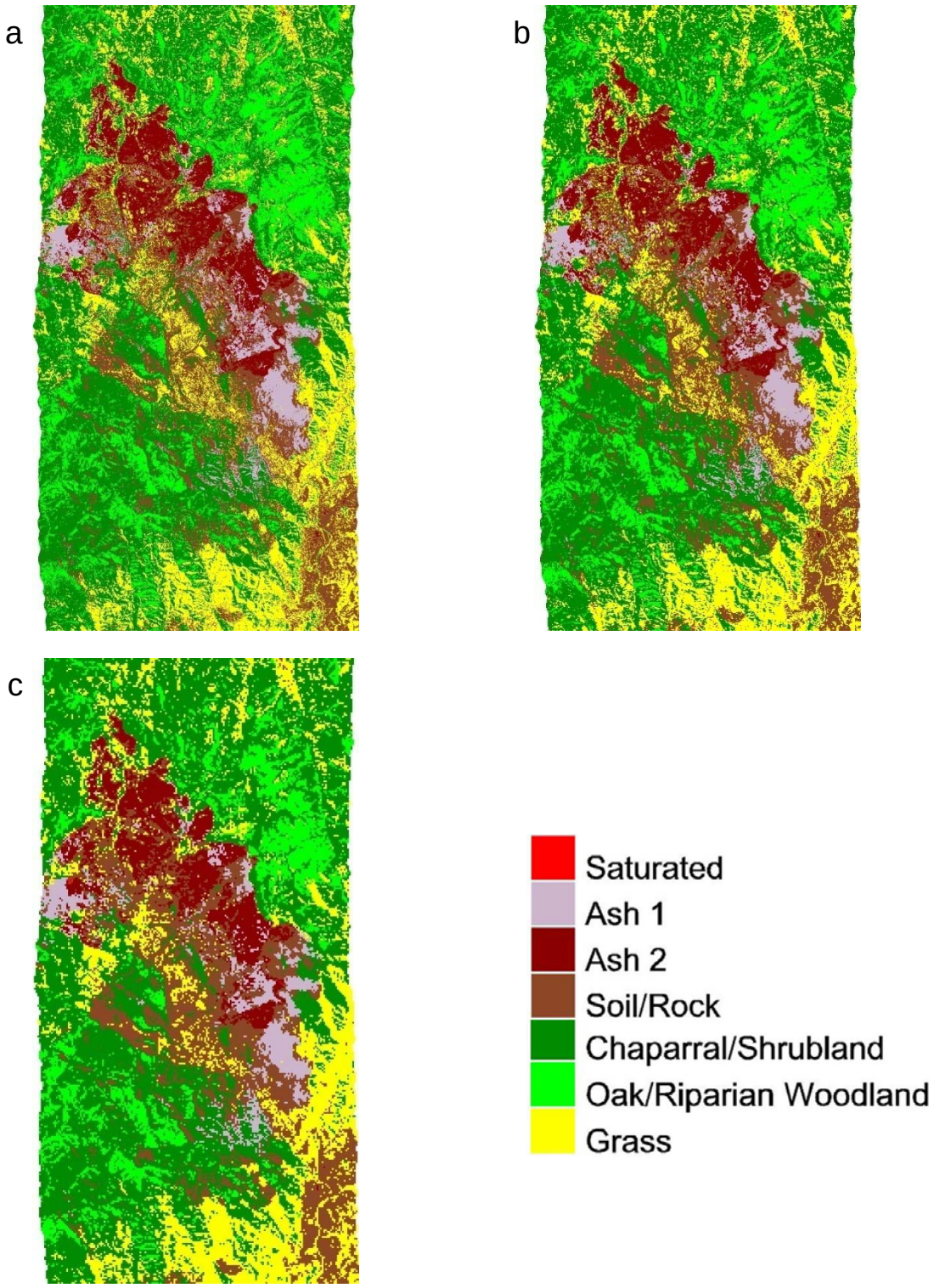

Figure 22. Background endmembers mapped for the Indians Fire scene at spatial resolutions of 16.1 m (a), 32.2 m (c), and 64.4 m (d). “Ash 1” lacks SWIR absorption features, and “Ash 2” exhibits apparent lignocellulose absorption.

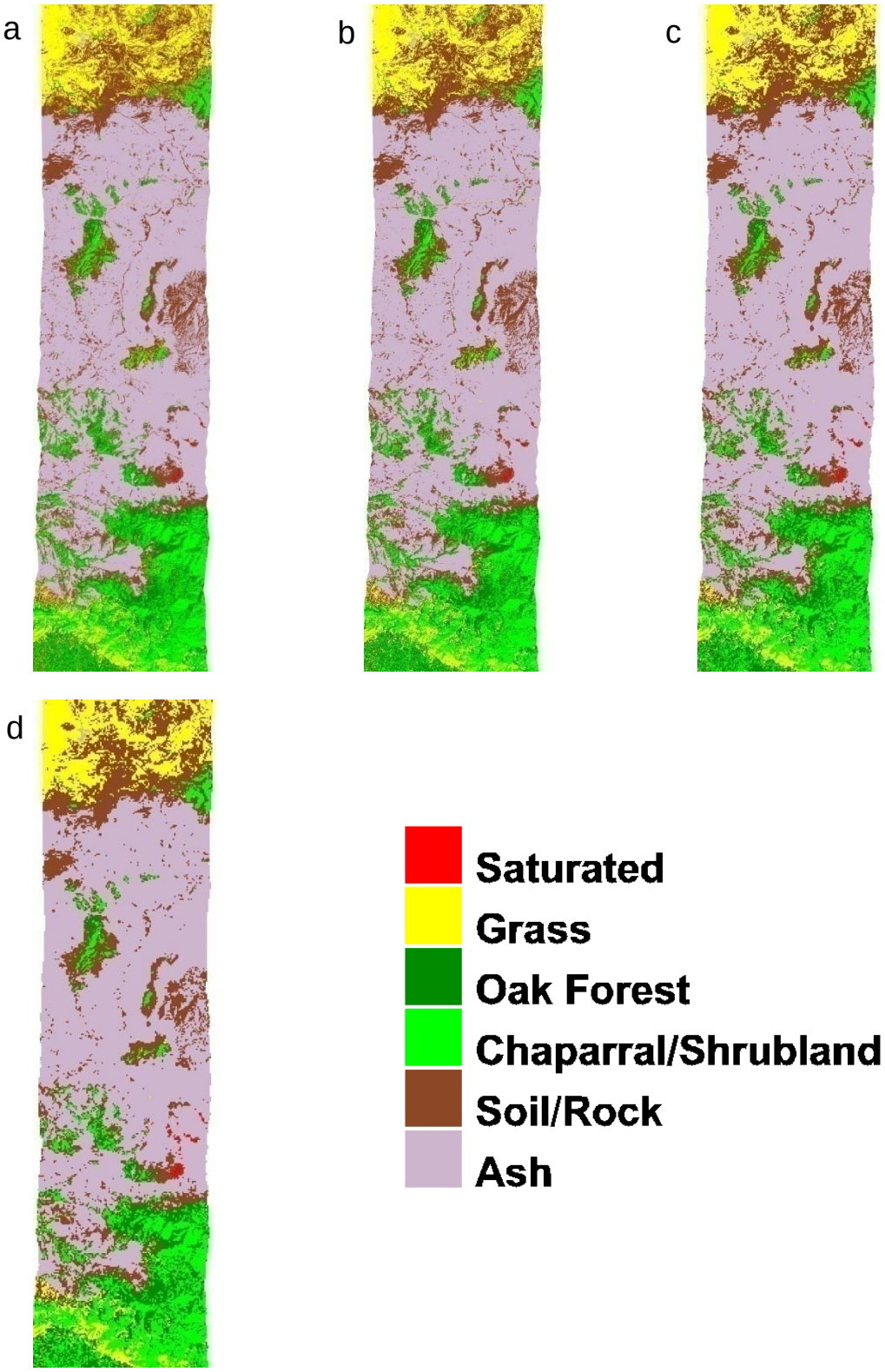

Figure 23. Background endmembers mapped for the Station Fire scene at spatial resolutions of 10.7 m (a), 21.4 m (b), 42.8 m (c), 64.2 m and (d).

5 DISCUSSION

Coarsening spatial resolution did have an effect on modeled fire area and temperature, although the general distributions of temperature and fire fractional area remained similar. Modeling at coarser resolutions produced larger areas of low fire temperature with lower modeling error. During spatial resampling, the radiance spectra of many smaller pixels (4, 16, 64, or 256) were averaged into those of a single larger pixel. Smaller pixels with higher radiance values from hotter fire temperatures were averaged with more numerous lower radiance values from cooler fires and nonfire background reflected radiance. This explains the increase in modeled fire fractional area for cooler temperatures as spatial resolution coarsened. Hotter temperatures were still modeled at coarser resolutions, although the modeled fractional area for these temperatures remained low, comparable to the area modeled for finer spatial resolutions.

One of the limitations of temperature modeling is the assumption of single temperature blackbody emission, even though fire is spatially and temporally dynamic and highly variable across the smallest of spaces. The emitted radiance measured within a single pixel can come from multiple combusting fuel elements, even at very high spatial resolutions. Thus, modeled temperature is an effective temperature based on the shape of emitted radiance and should not be directly equated with the kinetic temperature of the fire. Decreases in RMSE with coarsening spatial resolution indicate that fire emission may more closely resemble blackbody emission when radiance is averaged over larger areas. Collection of *in situ* data could improve understanding of the spatial distribution of

fire temperature and emitted radiance. Odion and Davis (2000) evaluated fire temperature and soil heating in chaparral stands using Tempilac paints, which melt at specific temperatures, on the soil surface (Tempil, Plainfield, New Jersey, USA). While fire temperatures fluctuate at different heights from the surface (Brooks, 2002), the use of temperature sensitive materials or thermocouples within a stand of burning vegetation could offer a reasonable first approach to surveying *in situ* temperature variability.

Saturation of the AVIRIS instrument had a major impact on modeling, especially at coarser spatial resolutions where longer wavelength bands were frequently masked. While the saturation mask ensured that saturated bands in high radiance pixels were excluded from modeling, it also resulted in a loss of valid information when the same bands were discarded from adjacent nonsaturated pixels included in the resampling. The AVIRIS saturation threshold in the SWIR as evaluated from the Simi Fire data was approximately 30 $\mu W\ cm^{-2}\ sr^{-1}\ nm^{-1}$. To find a more appropriate saturation threshold for the HyspIRI VSWIR instrument, temperature and fractional area from the Simi Fire 60.0 m Gaussian resampled data were used to calculate blackbody emission spectra for all bands. The pixel with the highest emitted radiance possessed a temperature of 940 K and a fire fractional area of 81%. Peak radiance for a blackbody with these characteristics occurs in the SWIR at 178 $\mu W\ cm^{-2}\ sr^{-1}\ nm^{-1}$ when accounting for the modeled atmospheric conditions for the Simi Fire AVIRIS image. Therefore, an ideal SWIR saturation threshold for HyspIRI VSWIR should be at least higher than this radiance value. It should be noted that this threshold was calculated from unsaturated bands. A higher threshold might result if data from bands saturated by the hottest areas of the four

fires could be analyzed, although these hot spots would also likely have low fractional areas within a 60.0 m pixel.

Spectral averaging with spatial resampling also had an effect on background endmember modeling. Variability of land cover was reduced in coarser resolution images when compared to finer resolutions. The broad land cover characteristics did remain consistent across all spatial resolutions, and confusion between widely different land cover types (e.g., oak forest vs. soil/rock) were rare, even for the coarsest resolution data for each fire scene. Classification accuracies were not assessed due to the lack of *in situ* data for all fires. Additionally, this study did not examine the use of endmembers retrieved from coarser spatial resolutions in the MESMA modeling. Endmember selection from finer spatial resolutions can improve overall accuracy (Clarke et al., 2001), while selection from coarser resolutions can decreases accuracy (Schaaf et al., in review). Relatively lower accuracy may therefore be expected when modeling with endmembers selected from resolutions closer to 60.0 m, but this remains to be tested, since no pre-fire *in situ* reference data existed for the fires used in this study.

RMSE decreased with coarsening spatial resolution. This implies that the spatially averaged spectra more closely resemble the spectral shape of a single temperature-emitting blackbody than spectra at finer resolutions. A caveat must be introduced here, since for temperatures at or higher than 1100 K, often only a single pixel was modeled from the coarsest resolution of each fire scene. For example, for each of the two 60.0 m subsets of the Simi Fire, only four bands were used to model a single pixel with 1190 K spectra (Table 6). The modeling algorithm ensured that at least two bands remained unsaturated to model temperature; however, Eckmann et al. (2008) recommended that a

minimum of four bands be used for temperature modeling. While the high spatial and spectral resolutions of AVIRIS data lend themselves well to modeling temperature even with only two bands, it is recommended that future MESMA modeling with HyspIRI data uses a minimum of four unsaturated bands to adjust for HyspIRI's coarser spatial resolution. Alternately, by adjusting the saturation thresholds of HyspIRI's SWIR spectral channels, as previously suggested, less saturation would occur, resulting in a higher number of bands left unsaturated for modeling temperature.

6 CONCLUSIONS

This study examined the performance of HFDI fire detection and MESMA temperature modeling across multiple spatial resolutions of four AVIRIS datasets containing actively burning wildfires. A saturation mask was used to ensure that saturated spectra would not distort radiance values in the spatially aggregated data. Spatial aggregation was compared to a more accurate Gaussian point spread function at 60.0 m resolution, and the two resampling techniques were found to produce similar results. Modeling results supported the viability of hyperspectral fire detection and temperature modeling of data with spatial resolutions similar to HyspIRI's proposed 60.0 m by 60.0 m pixel dimensions. No threshold within the spatial range of 4.0 – 60.0 m was detected for the four images that limited the reasonable performance of HFDI and MESMA modeling. That being stated, coarser hyperspectral data, such as that collected by the future HyspIRI sensor, may be expected to model more fire area at lower temperatures when compared against simultaneously acquired higher spatial resolution data.

Wildfires are complex and hazardous, and can produce both devastating and renewing effects on human and natural systems. Remote sensing is one of the better tools for observing wildfire, but cannot by itself assess or anticipate fire behavior. When used in conjunction with in situ data and lab measurements, however, remotely sensed data may provide snapshots of fire patterns that can be used to better understand and more effectively manage wildfire as a physical phenomenon.

Hyperspectral data, particularly in the SWIR region of the spectrum, are critical to modeling the emitted radiance of wildfires. The proposed HyspIRI sensor promises vastly superior temporal resolution to AVIRIS, providing lower cost global coverage that will allow for more dynamic analysis of wildfire temperature patterns, burn severity, and post-fire succession. Further research in these areas can further improve modeling of wildfire properties. Adjustments to saturation thresholds in SWIR channels on the HyspIRI VSWIR sensor—higher than 178 $\mu W\ cm^{-2}\ sr^{-1}\ nm^{-1}$ based on modeled temperatures and fractions from one AVIRIS scene—could ultimately provide more unsaturated bands for more effective fire detection and temperature modeling.

LITERATURE CITED

Adams, J. B., Smith, M. O., & Gillespie, A. R. (1993). Imaging spectroscopy: Interpretation based on spectral mixture analysis. In C. M. Pieters, & P. A. J. Englert (Eds.), *Remote geochemical analysis: Elemental and mineralogical composition* (145–166). Cambridge, England: Press Syndicate of University of Cambridge.

Anderson, M. C., Kustas, W. P., & Norman, J. M. (2007). Upscaling flux observations from local to continental scales using thermal remote sensing. *Agronomy Journal, 99*, 240 – 254.

Bian, L. (1997). Multiscale nature of spatial data in scaling up environmental models. In D. A. Quattrochi & M. F. Goodchild (Eds.), *Scale in remote sensing and GIS* (13 – 26). Boca Raton, FL: Lewis Publishers.

Boardman, J. W. (1999). Precision geocoding of low altitude AVIRIS data: Lessons learned in 1998. *Summaries of the eighth JPL Airborne Earth Science Workshop, 99 – 17*. (pp. 63 – 68) Pasadena: Jet Propulsion Laboratory, JPL Publication.

Brooks, M. L. (2002). Peak fire temperatures and effects on annual plants in the Mojave Desert. *Ecological Applications, 12*(4), 1088 – 1102.

California Department of Forestry and Fire Protection (2009). Incident Information. http://cdfdata.fire.ca.gov/incidents/incidents.

Dennison, P. E. (2006). Fire detection in imaging spectrometer data using atmospheric carbon dioxide absorption, *International Journal of Remote Sensing, 27*(14), 3049 – 3055.

Dennison, P. E., Charoensiri, K., Roberts, D. A., Peterson, S. H., & Green, R. O. (2006). Wildfire temperature and land cover modeling using hyperspectral data. *Remote Sensing of Environment, 100*, 212 – 222.

Dennison, P. E., & Roberts, D. A. (2009). Daytime fire detection using airborne hyperspectral data. *Remote Sensing of Environment, 113*, 1646 – 1657.

Dennison, P. E., & Matheson, D.S. (2011). Comparison of fire temperature and fractional area modeled from SWIR, MIR, and TIR multispectral and SWIR hyperspectral airborne data. *Remote Sensing of Environment, 115*, 876 – 886.

Dozier, J. (1981). A method for satellite identification of surface temperature fields of subpixel resolution. *Remote Sensing of Environment*, *11*, 221 – 229.

Drewa, P. B., Platt, W. J., & Moser, E. B. (2002). Fire effects on resprouting of shrubs in headwaters of Southeastern longleaf pine savannahs. *Ecology*, *83*, 755 – 767.

Eckmann, T. C., Roberts, D. A., & Still, C. J. (2008). Using multiple endmember spectral mixture analysis to retrieve subpixel fire properties from MODIS. *Remote Sensing of Environment*, *112*, 3773 – 3783.

Eckmann, T. C., Roberts, D. A., & Still, C. J. (2009). Estimating subpixel fire sizes and temperatures from ASTER using multiple endmember spectral mixture analysis. *International Journal of Remote Sensing*, *30*(*22*), 5851 – 5864.

Eckmann, T. C., Still, C. J., Roberts, D. A., & Michaelsen, J. C. (2010). Variations in subpixel fire properties with season and land cover in Southern Africa. *Earth Interactions*, *14-006*.

Giglio, L., & Kendall, J. D. (2001). Application of the Dozier retrieval to wildfire characterization – A sensitivity analysis. *Remote Sensing of Environment*, *77*, 34 – 49.

Giglio, L., Descloitres, J., Justice, C. O., & Kaufman, Y. J. (2003). An enhanced contextual fire detection algorithm for MODIS. *Remote Sensing of Environment*, *87*, 273 – 282.

Green, R. O. (1996). Estimation of biomass fire temperature and areal extent from calibrated AVIRIS spectra. *Summaries of the Sixth Annual JPL Airborne Earth Science Workshop, Pasadena: Jet Propulsion Laboratory 96-4*(1) 105 – 113.

Green, R. O. (2009). HyspIRI : VSWIR science measurement baseline. Presentation at the *Second HyspIRI NASA Decadal Survey Mission Science Workshop: Pasadena, CA*. Retrieved from http://hyspiri.jpl.nasa.gov/downloads/public/2009_Workshop/day1/day1_3._Green_%20pres_HyspIRI_VSWIR_Sci_Meas_Green_090811.pdf

Hoefen, T. M., Kokaly, R. F., Green, R. O., Swayze, G. A., Plumlee, G. S. (2010). Post-wildfire surface material mapping using hyperspectral data, Station Fire, Southern California, USA. *General Assembly 2010*, European Geosciences Union, Vienna, Austria. May 2010. Conference Presentation.

Jensen, J. R. (2007). Remote sensing of environment: An earth resource perspective (2nd ed.). Upper Saddle River, NJ: Prentice Hall.

Kokaly, R. F., Rockwell, B. W., Haire, S. L., King, T. V.V. (2007). Characterization of post-fire surface covers, soils, and burn severity at the Cerro Grande Fire, New Mexico, using hyperspectral and multispectral remote sensing. *Remote Sensing of Environment 106*, 305 – 325.

National Interagency Fire Center (2010). Fire information – Wildland fire statistics. http://www.nifc.gov/fire_info/fire_stats.htm

National Research Council Committee on Earth Science and Applications from Space (2007). Earth science and applications from space: National imperatives for the next decade and beyond. Washington, D.C.: National Academies Press.

Nelson, M. D., McRoberts, R. E., Holden, G. R., & Bauer, M. E. (2009). Effects of satellite image spatial aggregation and resolution on estimates of forest land area. *International Journal of Remote Sensing, 30*(8), 1913 – 1940.

Odion, D. C., & Davis, F. W. (2000). Fire, soil heating, and the formation of vegetation patterns in chaparral. *Ecological Monographs, 70*(1), 149 – 169.

Rahman, A. F., Gamon, J. A., Sims, D. A., & Schmidt, M. (2003). Optimum pixel size for hyperspectral studies of ecosystem function in southern California chaparral and grassland. *Remote Sensing of Environment, 84*, 192 – 207.

Riaño, D., Meier, E., Allgöwer, B., Chuvieco, E., & Ustin, S. L. (2003). Modeling airborne laser scanning data for the spatial generation of critical forest parameters in fire behavior modeling. *Remote Sensing of Environment*, *86*, 177 – 186.

Roberts, D. A., Gardner, M., Church, R., Ustin, S., Scheer, G., & Green, R. O. (1998). Mapping chaparral in the Santa Monica Mountains using multiple endmember spectral mixture models. *Remote Sensing of Environment*, *65*, 267 – 279.

Schaaf, A. N., Dennison, P. E., Fryer, G. K., Roth, K. L. & Roberts, D. A. (In Press). Using hyperspectral data to classify vegetation at the plant functional type-level in mountain terrain at three spatial resolutions. *GIScience and Remote Sensing*.

Vane, G., Chrisp, M., Enmark, H., Macenka, S., Solomon, J. (1984). Airborne Visible/Infrared Imaging Spectrometer (AVIRIS): An advanced tool for earth remote sensing. In *Proceedings of the 1984 IEEE International Geoscience and Remote Sensing Symposium, Institute of Electrical and Electronics Engineers: New York, 215*, 751–757.

Vodacek, A., Kremens, R. L., Fordham, A. J., Vangorden, S.C., Luisi, D., Schott, J. R. & Latham, D. J. (2002). Remote optical detection of biomass burning using a potassium emission signature. *International Journal of Remote Sensing*, *13*, 2721 – 2726.

Walsh, S. J., Moody, A., Allen, T. R., & Brown, D. G. (1997) In D. A. Quattrochi & M. F. Goodchild (Eds.), *Scale in remote sensing and GIS* (27 – 56). Boca Raton, FL: Lewis Publishers.